# A STUDY OF LINE SOURCE FIELDS
# TRANSMITTED THROUGH A 2D CIRCULAR
# DIELECTRIC RADOME OR A SLAB

## A THESIS

SUBMITTED TO THE DEPARTMENT OF ELECTRICAL AND
ELECTRONICS ENGINEERING
AND THE INSTITUTE OF ENGINEERING AND SCIENCES
OF BILKENT UNIVERSITY
IN PARTIAL FULFILLMENT OF THE REQUIREMENTS
FOR THE DEGREE OF
MASTER OF SCIENCE

By
Anıl Bircan
August 1996

# A STUDY OF LINE SOURCE FIELDS TRANSMITTED THROUGH A 2D CIRCULAR DIELECTRIC RADOME OR A SLAB

A THESIS

SUBMITTED TO THE DEPARTMENT OF ELECTRICAL AND

ELECTRONICS ENGINEERING

AND THE INSTITUTE OF ENGINEERING AND SCIENCES

OF BILKENT UNIVERSITY

IN PARTIAL FULFILLMENT OF THE REQUIREMENTS

FOR THE DEGREE OF
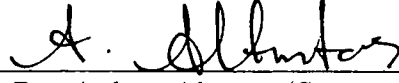MASTER OF SCIENCE

By

Anıl Bircan

August 1996

ANIL BIRCAN

tarafından bağışlanmıştır.

I certify that I have read this thesis and that in my opinion it is fully adequate, in scope and in quality, as a thesis for the degree of Master of Science.

_____
Prof. Dr. Ayhan Altıntaş(Supervisor)
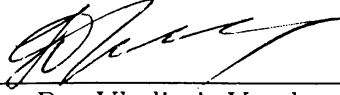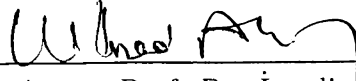
I certify that I have read this thesis and that in my opinion it is fully adequate, in scope and in quality, as a thesis for the degree of Master of Science.

_____
Dr. Vladimir Yurchenko

I certify that I have read this thesis and that in my opinion it is fully adequate, in scope and in quality, as a thesis for the degree of Master of Science.

_____
Assoc. Prof. Dr. İrşadi Aksun

I certify that I have read this thesis and that in my opinion it is fully adequate, in scope and in quality, as a thesis for the degree of Master of Science.

_____
Assist. Prof. Dr. Levent Gürel

Approved for the Institute of Engineering and Sciences:

_____
Prof. Dr. Mehmet Baray
Director of Institute of Engineering and Sciences

ii

# ABSTRACT

## A STUDY OF LINE SOURCE FIELDS TRANSMITTED THROUGH A 2D CIRCULAR DIELECTRIC RADOME OR A SLAB

Anıl Bircan
M.S. in Electrical and Electronics Engineering
Supervisor: Prof. Dr. Ayhan Altıntaş
August 1996

In this thesis, far field solutions for the real and complex line sources surrounded by a cylindrical dielectric shell (radome) are obtained in both $E$ and $H$ polarizations. These far fields for the radome model are then compared with the ones transmitted through an infinite dielectric slab.

The motivation is that as the far field in the main beam direction is concerned, the radome of large radius can be approximated by an infinite dielectric slab. It is clear that the fields of the cylindrical shell (radome) is expressed in terms of cylindrical functions whereas for the slab, the fields are given through Sommerfeld integrals. By applying the saddle point integration techniques to the Sommerfeld integrals, the radiated fields of the slab are numerically calculated and compared with the fields of the dielectric shell. The source is taken as a line source, but it can also simulate a beam field by the complex source approach.

The study gives a better understanding of the reflector antennas covered with dielectric radomes.

*Keywords : Dielectric Radome, Dielectric Slab, Complex Source*

# ÖZET

## DİELEKTRİK RADOM VE TABAKADAN GEÇEN DOĞRUSAL KAYNAK ALANLARININ İNCELENMESİ

Anıl Bircan
Elektrik ve Elektronik Mühendisliği Bölümü Yüksek Lisans
Tez yöneticisi: Prof. Dr. Ayhan Altıntaş
Ağustos 1996

Bu çalışmada, $E$ ve $H$ polarizasyonlarda, silindirik dielektrik kabukla (radom) çevrelenmiş reel ve karmaşık kaynaklar için Fraunhofer bölgesinde alan çözümleri bulunmuştur. Radom modeli için hesaplanan bu uzak bölge alanları, aynı kaynaklardan yayılan ve sonsuz dielektrik tabakadan geçen alanlar ile karşılaştırılmıştır.

Buradaki motivasyon, ana yayılma doğrultusu yönündeki uzak bölge alanları düşünüldüğünde, büyük yarıçaplı bir radomun sonsuz dielektrik tabaka ile modellenebileceğidir. Radom modelindeki alanların silindirik fonksiyonlar cinsinden bulunacağı açıktır. Düzlem modeli için ise Sommerfeld integrali kullanılmıştır. Eyer noktası integrasyon teknikleri kullanılarak Sommerfeld integralleri çözülmüş ve tabaka modelindeki alanlar radom modeli için hesaplanmış alanlar ile karşılaştırılmıştır. Kaynak çizgisel (2 boyutta noktasal) alınmış ancak pratikteki doğrultulmuş antenleri simule edebilmesi için karmaşık kaynak yaklaşımı uygulanmıştır.

Bu tez, dielektrik radomla çevrelenmiş yansıtıcı antenlerin daha iyi anlaşılmasını sağlamaktadır.

*Anahtar Kelimeler : Dielektrik Radom. Dielektrik Tabaka. Karmaşık Kaynak*

# ACKNOWLEDGMENTS

·

# TABLE OF CONTENTS

# LIST OF FIGURES

# Chapter 1

# INTRODUCTION

The penetration of electromagnetic waves through dielectric layers is an interesting concern, for instance in the performance of antennas surrounded by radomes. A radome is a dielectric shell used to protect the antenna from water, sun, wind, etc. The radome, however, distorts the radiation pattern in the far field by the peak-gain attenuation (loss of peak gain) and the boresight error (difference between the apparent and the distorted beam directions) [1]. A precise analysis of radome performance is difficult, and nearly impossible in practice, because the general shape of a radome layer does not fit into the frame suitable for exact analysis. Thus, some approximation methods are resorted in the literature. The basic principle of approximation is to find a configuration to approximate the surface of the dielectric layer locally, which can be solved rigorously by analytic means.

Plane wave spectral decomposition of the incident field, local plane wave tracking through an equivalent plane slab and spectral synthesis of the transmitted field procedures ignore at least the surface curvature when using equivalent local slab models or multiple internal reflections and guided and leaky waves excited in the radome [2]. In [2], a curvature corrected slab transmission coefficient is given. Then, high frequency asymptotics, ray approach and physical optics with the coefficients found in [2] are used [3] to solve the radiation from radome covered antennas. Ray techniques are used again for narrow waisted Gaussian beam propagation through dielectric plane layer and circular cylindrical layer [4]. In [5], attention is focused on the relation between Green's functions appropriate to closed and open shells; the $0 - 2\pi$ (periodic) and $(-\infty) - (+\infty)$ (nonperiodic) dependencies and the equivalence relation

between partial angular harmonic and ray type Green's functions are investigated. Accuracy, interrelation between the solutions and comparing them with reliable tests are studied.

In this work, for the radome and slab geometries, real (axial) line sources in both $E$ and $H$ polarizations are taken into account, and, additionally, complex line sources are considered to simulate directed beam fields used in practice. For the closed, circular geometry of the radome, cylindrical functions are used to represent the incident field via the addition theorem and the scattered fields in the inner, outer and the middle regions. Then the boundary conditions are applied to the total fields to obtain the Green's functions. For the open, infinite structure of the dielectric slab, the spectral representation is used to calculate the far field. The Sommerfeld integral is carried out by asymptotics with the surface wave contribution. The frequency and the thickness variations of the models are also examined to understand better the nature of the radome and the slab structures. Finally, the far fields obtained for both models are compared to study the validity of approximation of the radome by a dielectric slab.

The outline of this thesis is as follows: In Chapter 2, the radome geometry and problem are formulated and the solution is given. The solution involves Bessel functions whose numerical generation is described in Chapter 3. In Chapter 4, the infinite dielectric slab is considered. The Green's functions for both models are compared and the field difference is analyzed numerically in Chapter 5. Main conclusions are given in Chapter 6.

In the analysis, a sinusoidally-varying time dependence $e^{-iwt}$ is assumed and suppressed.

# Chapter 2

# THE FAR FIELDS OF THE DIELECTRIC CIRCULAR SHELL (RADOME)

## 2.1 Real Line Source

A line current which is directed along the z axis, is assumed to be placed at $\vec{r'}$ as shown in Figure 2.1. The inner and outer radii are shown by $c$ and $d$, respectively. The radome divides the whole space into three distinct regions as shown in the figure. The radome material is assumed to be dielectric with $\epsilon_1$ and the radome is located in free space. From the symmetry, $\vec{r'}$ is taken as directed along x-axis without loss of generality. The incident field radiated by the source is uniform and axially symmetric with respect to the source position $\vec{r'}$:

$$U^{inc} = H_0^{(1)}(k_0|\vec{r} - \vec{r'}|). \tag{2.1}$$

where $k_0$ is the free space wavenumber.

The scattered fields can be written as

$$U_1^{sc} = \sum_{n=-\infty}^{\infty} s_n J_n(k_0 r) e^{in\phi}, \quad r \leq c. \tag{2.2}$$

3
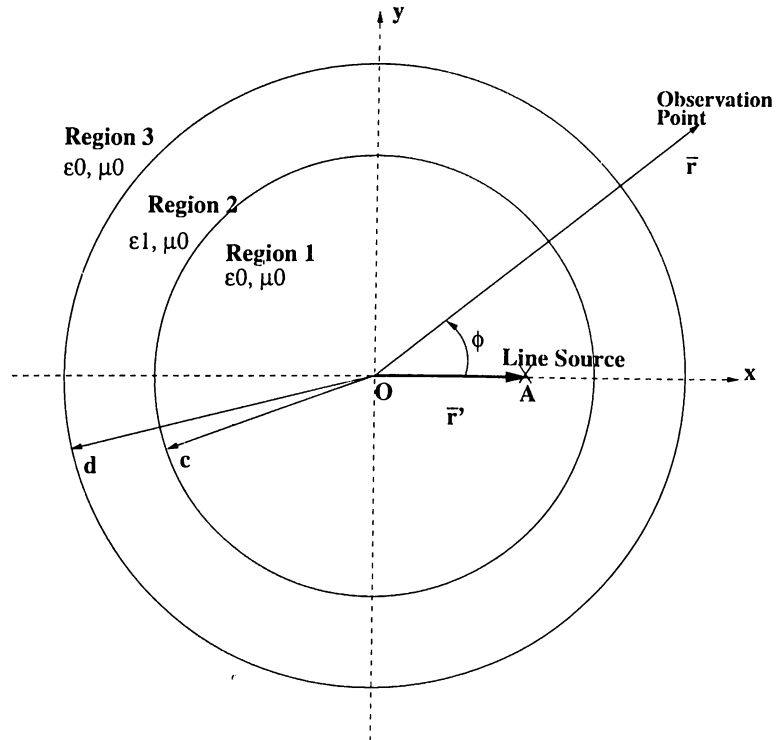
Figure 2.1: Radome Geometry. The inner and outer radii are given by c and d, respectively. $\vec{r'}$ is used as the location vector for real line source. For simplicity, $\vec{r'}$ is assumed to be directed along the x-axis.

$$U_2^{sc} = \sum_{n=-\infty}^{\infty} [\bar{p}_n J_n(k_1 r) + \bar{q}_n H_n^{(1)}(k_1 r)] e^{in\phi}, \quad c \le r \le d, \tag{2.3}$$

$$U_3^{sc} = \sum_{n=-\infty}^{\infty} \bar{r}_n H_n^{(1)}(k_0 r) e^{in\phi}, \quad r \ge d, \tag{2.4}$$

where $k_1 = k_0\sqrt{\epsilon_r}$ is the wavenumber in the radome and $U_1^{sc}$, $U_2^{sc}$, $U_3^{sc}$ are the z-components in Regions 1,2,3 of either electric or magnetic field in the case of $E$ or $H$ polarization, respectively.

Note that, for the scattered fields, only standing waves ($J'_n s$) in Region 1, outgoing ($H'_n s$) and standing waves in Region 2 and only outgoing waves in Region 3 (since no reflection occurs in this region) are included. Using the addition theorem, the incident field can be written in the form of a series:

|

$$U^{inc} = H_0^{(1)}(k_0|\vec{r} - \vec{r'}|) = \begin{cases} \sum_{n=-\infty}^{\infty} H_n^{(1)}(k_0r')J_n(k_0r)e^{in(\phi-\phi')}, & r < r' \\ \sum_{n=-\infty}^{\infty} H_n^{(1)}(k_0r)J_n(k_0r')e^{in(\phi-\phi')}, & r > r', \end{cases} \quad (2.5)$$

where $\phi'$ must be taken as zero, since $\vec{r'}$ is along the x-axis. Thus the total field is determined by the expansion

$$U_1^{tot} = U_1^{sc} + U^{inc} = \begin{cases} \sum_{n=-\infty}^{\infty}[s_n + H_n^{(1)}(k_0r')]J_n(k_0r)e^{in\phi}, & 0 < r < r' \\ \sum_{n=-\infty}^{\infty}[s_nJ_n(k_0r) + J_n(k_0r')H_n^{(1)}(k_0r)]e^{in\phi}, & r' < r \leq c, \end{cases}$$
$$(2.6)$$

in Region 1, and by the expressions (2.7) and (2.8) in Regions 2 and 3 respectively,

$$U_2^{tot} = \sum_{n=-\infty}^{\infty}[p_nJ_n(k_1r) + q_nH_n^{(1)}(k_1r)]e^{in\phi}, \quad c \leq r \leq d, \quad (2.7)$$

$$U_3^{tot} = \sum_{n=-\infty}^{\infty} r_nH_n(k_0r)e^{in\phi}, \quad r \geq d, \quad (2.8)$$

where $s_n$, $p_n$, $q_n$ and $r_n$ are the coefficients to be determined by the boundary conditions.

In the case of $E$ polarization, the continuity of $E_z$ and $H_\phi = \frac{i}{w\mu}\frac{\partial E_z^{tot}}{\partial r}$ (tangential fields) at the boundaries $r = c, d$ and the orthogonality conditions give an infinite set of equations. This set consists of a series of independent blocks in four equations:

$$E_1^{tot} = E_2^{tot}|_{r=c} \Rightarrow s_nJ_n(k_0c) + J_n(k_0r')H_n^{(1)}(k_0c) = p_nJ_n(k_1c) + q_nH_n^{(1)}(k_1c),$$
$$(2.9)$$

$$E_2^{tot} = E_3^{tot}|_{r=d} \Rightarrow r_nH_n(k_0d) = p_nJ_n(k_1d) + q_nH_n^{(1)}(k_1d), \quad (2.10)$$

$$H_1^{tot} = H_2^{tot}|_{r=c} \Rightarrow s_nJ_n'(k_0c) + J_n(k_0r')H_n^{(1)\prime}(k_0c) = \sqrt{\epsilon_r}p_nJ_n'(k_1c) + \sqrt{\epsilon_r}q_nH_n^{(1)\prime}(k_1c),$$
$$(2.11)$$

$$H_2^{tot} = H_3^{tot}|_{r=d} \Rightarrow r_nH_n^{(1)\prime}(k_0d) = \sqrt{\epsilon_r}p_nJ_n'(k_1d) + \sqrt{\epsilon_r}q_nH_n^{(1)\prime}(k_1d) \quad (2.12)$$

with four unknown coefficients $r_n$, $p_n$, $q_n$ and $s_n$.

Solving this system, the coefficients are obtained, and so are the fields in all the regions.
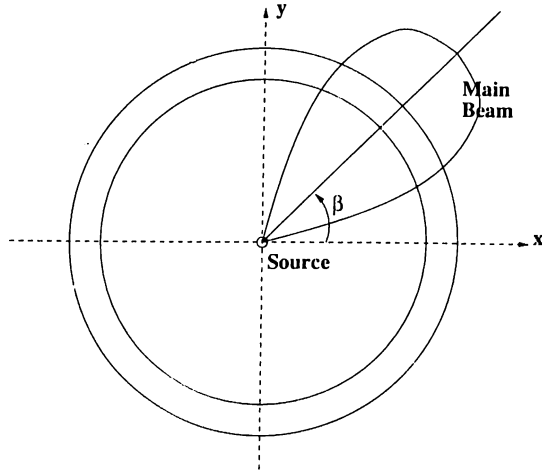
Figure 2.2: Geometry of the Complex Line Source Inside the Radome

Similarly, in the $H$ polarization, orthogonality and the continuity of $H_z$ and $E_\phi = \frac{i}{w\epsilon_0} \frac{\partial H_z^{tot}}{\partial r}$ at the boundaries give the equations with unknown coefficients $r_n$, $p_n$, $q_n$ and $s_n$:

$$H_1^{tot} = H_2^{tot}|_{r=c} \Rightarrow s_n J_n(k_0 c) + J_n(k_0 r') H_n^{(1)}(k_0 c) = p_n J_n(k_1 c) + q_n H_n^{(1)}(k_1 c),$$
$$(2.13)$$

$$H_2^{tot} = H_3^{tot}|_{r=d} \Rightarrow r_n H_n(k_0 d) = p_n J_n(k_1 d) + q_n H_n^{(1)}(k_1 d), \qquad (2.14)$$

$$E_1^{tot} = E_2^{tot}|_{r=c} \Rightarrow s_n J_n'(k_0 c) + J_n(k_0 r') H_n^{(1)\prime}(k_0 c) = \frac{1}{\sqrt{\epsilon_r}} [p_n J_n'(k_1 c) + q_n H_n^{(1)\prime}(k_1 c)],$$
$$(2.15)$$

$$H_2^{tot} = H_3^{tot}|_{r=d} \Rightarrow r_n H_n^{(1)\prime}(k_0 d) = \frac{1}{\sqrt{\epsilon_r}} [p_n J_n'(k_1 d) + q_n H_n^{(1)\prime}(k_1 d)]. \quad (2.16)$$

Again solving the system gives the coefficients and the fields. Examining the system of equations for both polarizations, one recognizes that the only difference is that the $\sqrt{\epsilon_r}$ coefficient appears in the other as $1/\sqrt{\epsilon_r}$.

## 2.2 Complex Line Source

Unlike the real line source, the antenna feeders are not uniform in practice. So, to simulate nonuniform radiators the complex line source is used, [6], [7]. In Figure 2.2, a complex line source in a radome with a beam is shown. The line source is placed at a complex location $\vec{r}_s$ which is given by

$$\vec{r_s} = \vec{r_0} + i\vec{b} = a\hat{x} + ib(\cos\beta\hat{x} + \sin\beta\hat{y}), \qquad (2.17)$$

where the parameter $\beta$ gives the direction of the beam and $b$ is related to the beamwidth. For $b = 0$, the source is real and radiation is uniform.

Assuming that the source is located at $(r_s, \theta_s)$, the field intensity at any observation point $(r, \theta)$ may be written as

$$U_z^{inc}(\vec{r}) = H_0^{(1)}(k_0 R) \simeq \sqrt{2/\pi}e^{-i\pi/4}\frac{e^{ik_0 R}}{\sqrt{k_0 R}}, \qquad k_0 R \gg 1, \qquad (2.18)$$

where $R$ is the distance of the observation point from the source,

$$R = \sqrt{r^2 + r_s^2 - 2rr_s\cos(\theta - \theta_s)}. \qquad (2.19)$$

In the far field, $R = r - r_0\cos(\theta - \theta_s)$ applies in the phase term, $R \sim r$ in the amplitude term of (2.18):

$$U_z^{inc} = C\frac{e^{ik_0(r - r_s\cos(\theta - \theta_s))}}{\sqrt{k_0 r}}, \qquad r \gg |r_s|. \qquad (2.20)$$

Here, $\vec{r_s}$, $\vec{r_0}$ and $\vec{b}$ are the complex source position, real source position and beam parameter vectors given in polar coordinates as $\vec{r_0} = (r_0, \theta_0)$, $\vec{r_s} = (r_s, \theta_s)$ and $\vec{b} = (b, \beta)$. All angles are measured from the x-axis. The values of $r_s$ and $\theta_s$ are

$$r_s = \sqrt{r_0^2 - b^2 + 2ib\cos\beta}, \qquad \theta_s = \cos^{-1}\left(\frac{r_0 + ib\cos\beta}{r_s}\right). \qquad (2.21)$$

Substituting (2.21) into (2.20) the following expression is obtained:

$$U_z^{inc} = C\frac{e^{ik_0(r - r_0\cos(\theta - \theta_0))}}{\sqrt{k_0 r}}e^{kb\cos(\theta - \beta)}, \qquad (2.22)$$

which yields a maximum at $\theta = \beta$ and a minimum at $\theta = \beta + \pi$.

The incident field can also be written as a series in terms of the addition theorem:

$$U_z^{inc}(\vec{r}) = C \; H_0^{(1)}(k_0|\vec{r} - \vec{r_s}|) = C \sum_{n=-\infty}^{\infty} J_n(k_0 r_s) H_n^{(1)}(k_0 r) e^{in(\phi - \theta_s)}, \quad r > |r_s|.$$

$$(2.23)$$

The complex source at $\vec{r_s}$ can be thought as a cylindrical source in real space located at $\vec{r} = \vec{r_0}$. $U_{inc}$ is an exact solution of the Helmholtz equation, this is unlike the Gaussian-type exponents frequently used to represent beam waves. Gaussian beam field is an approximate solution of the field equations that fails outside the paraxial region surrounding the beam axis, the complex-source-point yields a valid solution of the Helmholtz equation at arbitrary observation points.

Using the scattered fields given in (2.2), (2.3), (2.4), the total fields can be written as:

$$U_1^{tot} = \sum_{n=-\infty}^{\infty} [s_n J_n(k_0 r) + C \; J_n(k_0 r_s) H_n^{(1)}(k_0 r) e^{-in\theta_s}] e^{in\phi}, \quad r_s < r \le c, \quad (2.24)$$

$$U_2^{tot} = \sum_{n=-\infty}^{\infty} [p_n J_n(k_1 r) + q_n H_n^{(1)}(k_1 r)] e^{in\phi}, \quad c \le r \le d, \quad (2.25)$$

$$U_3^{tot} = \sum_{n=-\infty}^{\infty} r_n H_n^{(1)}(k_0 r) e^{in\phi}, \quad r \ge d. \quad (2.26)$$

Continuity of the tangential fields yields

$$s_n J_n(k_0 c) + C \; J_n(k_0 r_s) H_n^{(1)}(k_0 c) e^{-in\theta_s} = p_n J_n(k_1 c) + q_n H_n^{(1)}(k_1 c), \quad (2.27)$$

$$r_n H_n^{(1)}(k_0 d) = p_n J_n(k_1 d) + q_n H_n^{(1)}(k_1 d), \quad (2.28)$$

$$s_n J_n'(k_0 c) + C \; J_n(k_0 r_s) H_n^{(1)\prime}(k_0 c) e^{-in\theta_s} = \alpha[p_n J_n'(k_1 c) + q_n H_n^{(1)\prime}(k_1 c)], \quad (2.29)$$

$$r_n H_n^{(1)\prime}(k_0 d) = \alpha[p_n J_n'(k_1 d) + q_n H_n^{(1)\prime}(k_1 d)], \quad (2.30)$$

where $\alpha = \sqrt{\frac{\epsilon_r}{\mu_r}}$ in $E$ polarization and $\alpha = \sqrt{\frac{\mu_r}{\epsilon_r}}$ in $H$ polarization.

The field of interest is the one at far field which includes the coefficient $r_n$,

$$r_n = \frac{\alpha x_{2n} x_{7n}(x_{1n}y_{3n} - x_{3n}y_{1n})c_{1n}}{(x_{6n}y_{7n} - \alpha x_{7n}y_{6n})[x_{8n}c_{2n} - x_{7n}(x_{1n}y_{5n} - \alpha x_{5n}y_{1n})] + x_{6n}c_{2n}c_{1n}}, \quad (2.31)$$

where

$$c_{1n} = x_{7n}y_{8n} - x_{8n}y_{7n}, \quad c_{2n} = x_{1n}y_{4n} - \alpha x_{4n}y_{1n}, \quad (2.32)$$

$$x_{1n} = J_n(k_0 c), \quad y_{1n} = J_n'(k_0 c), \quad (2.33)$$

$$x_{2n} = C \ J_n(k_0 r_s)e^{-in\theta_s}, \quad (2.34)$$

$$x_{3n} = H_n^{(1)}(k_0 c), \quad y_{3n} = H_n'^{(1)}(k_0 c), \quad (2.35)$$

$$x_{4n} = J_n(k_1 c), \quad y_{1n} = J_n'(k_1 c), \quad (2.36)$$

$$x_{5n} = H_n^{(1)}(k_0 c), \quad y_{5n} = H_n^{(1)'}(k_0 c), \quad (2.37)$$

$$x_{6n} = H_n^{(1)}(k_0 d), \quad y_{6n} = H_n^{(1)'}(k_0 d), \quad (2.38)$$

$$x_{7n} = J_n(k_1 d), \quad y_{7n} = J_n'(k_1 d), \quad (2.39)$$

$$x_{8n} = H_n^{(1)}(k_1 d), \quad y_{8n} = H_n^{(1)'}(k_1 d) \ . \quad (2.40)$$

In the numerical implementation of the radome geometry fields, Bessel functions are generated as described in the next chapter. The radius, thickness and the dielectric constant of the radome determine the truncation number of the series expansions of the fields.

# Chapter 3

# NUMERICAL GENERATION OF CYLINDRICAL FUNCTIONS

## 3.1 Introduction

In this chapter, the numerical computation of Bessel functions of the first and second kind for integer orders and complex arguments are considered.

Bessel functions of integer order are the natural and general solutions of many radiation, scattering and guided wave problems which are formulated in the cylindrical coordinate system. Complex or imaginary arguments are associated with lossy materials, evanescent fields and leaky waves for instance. Bessel functions are also used in the mathematical description of numerous physical phenomena besides electromagnetism. Consequently their accurate computation is of general importance.

$J_n(x)$ and $Y_n(x)$, Bessel functions of the first and second kind respectively are solutions to Bessel's differential equations

$$z^2\, y'' + z\, y' + (z^2 - n^2)y = 0. \tag{3.1}$$

One way to represent $J_n(z)$ and $Y_n(z)$ for integer $n$ is [9],

$$J_n(z) = (z/2)^n \sum_{k=0}^{\infty} \frac{(-z^2/4)^k}{k!(n+k)!}, \tag{3.2}$$

$$
\begin{aligned}
Y_n(z) &= \frac{2}{\pi} \ln(z/2) J_n(z) - \frac{(z/2)^{-n}}{\pi} \sum_{k=0}^{n-1} \frac{(n-k-1)!}{k!}(z^2/4)^k \\
&\quad - \frac{(z/2)^n}{\pi} \sum_{k=0}^{\infty} [\varphi(k+1) + \varphi(n+k+1)] \frac{(-z^2/4)^k}{k!(n+k)!}, \tag{3.3}
\end{aligned}
$$

where $\varphi(m) = -\tau + \sum_{k=1}^{m-1} 1/k$ with $\varphi(1) = -\tau$, and $\tau$ is Euler's constant.

Using these equations to determine $J_n(z)$ and $Y_n(z)$ is impractical because serious losses of significance caused by small differences of large numbers occur when the terms in the summations become too large. Alternatively an integral representation may be tried for $J_n(z)$

$$J_n(z) = \frac{1}{\pi} \int_0^{\pi} \cos(z \sin \theta - n\theta) d\theta, \tag{3.4}$$

but the integrand oscillates rapidly for large arguments and orders, this requires many steps in the numerical integration, causing the computation time to be too long.

Instead of these rather unsuitable methods of obtaining Bessel functions, a different approach is applied in this thesis. It utilizes the method given by DuToit [8] which encounters some forward and backward iterations based on the recurrence relation

$$B_{n+1}(z) = \frac{2n}{z} B_n(z) - B_{n-1}(z). \tag{3.5}$$

It is the main equality which enables the calculation of $J_n(z)$ and $Y_n(z)$ of all orders for a given argument z, when two consequtive orders $B_q(z)$ and $B_{q+1}(z)$ are known.

Before using this relation, the stability of recurrence should be guaranteed. When the forward recurrence is used, the factor $2n/z$ amplifies any round-off error. With the repetitive use of (3.5) the accumulation of errors occurs. The relative errors are, however, decreasing when the functions $B_n$ are increasing in the process of iteration. So, progressing through increasing values of $|B_n(z)|$ appears to be the best strategy.

Therefore, for $J_n(z)$ functions, the backward recurrence is stable since
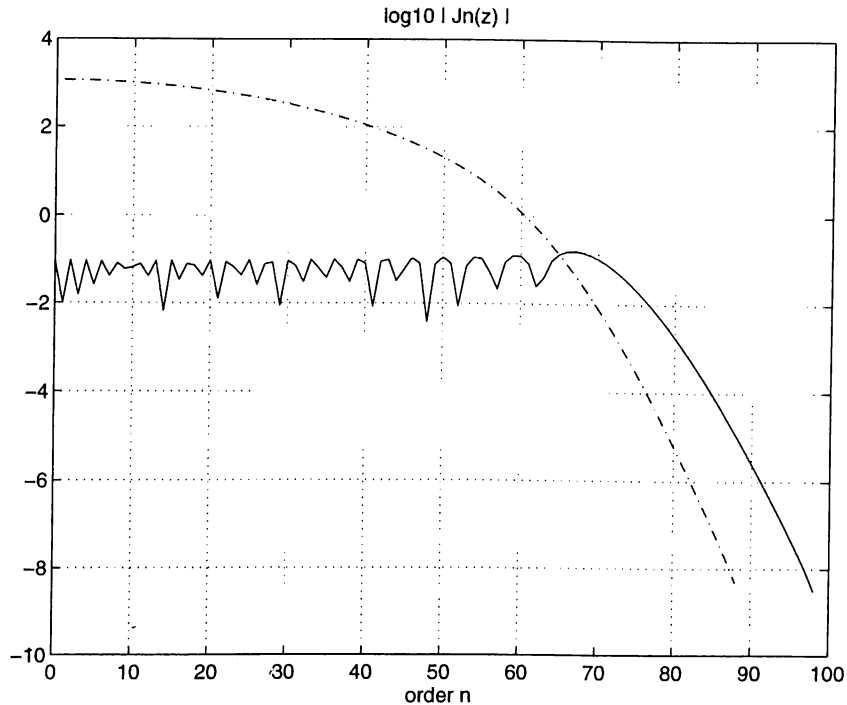
Figure 3.1: $|J_n(z)|$, Argument: $z = 70 + 0i$ solid line, $z = 60 + 10i$ dash-dotted line

$|J_n(z)|$ are increasing rapidly with decreasing $n$. For $Y_n(z)$, when $z$ is complex, the backward recurrence is stable for small $n$ but the forward recurrence is needed for $n > r$ where $r$ is the index corresponding to the minimum of $|Y_n(z)|$.

Numerical experimentation indicated that the relative propagated error is always stable when this rule is followed, see Figures 3.1 and 3.2 .

In more details, the guidelines are as follows:

1. When z is real or when $|Re(z)| \gg |Im(z)|$, the general magnitude of $|J_n(z)|$ and $|Y_n(z)|$ is approximately constant for a given argument $z$ for $n < |z|$. The relative propagated error is stable under these conditions when recurrence is carried out with either increasing n (forward recurrence) or decreasing n (backward recurrence). Since $J_n(z)$ decreases with increasing $n$ when $n > |z|$ (Fig. 3.1), backward recurrence can be used starting with arbitrary initial orders $J_q(z)$ and $J_{q+1}(z)$ to compute the lower orders. Since $Y_n(z)$ increases with $n$ when $n > |z|$ (Fig. 3.2) all higher orders may be computed from $Y_0(z)$ and $Y_1(z)$, using forward recurrence.

2. When z is complex, the same rule still applies for $J_n(z)$, since it decreases with increasing n for all values of $n$. $Y_n(z)$ can be calculated from $Y_r(z)$, $Y_{r+1}(z)$

12
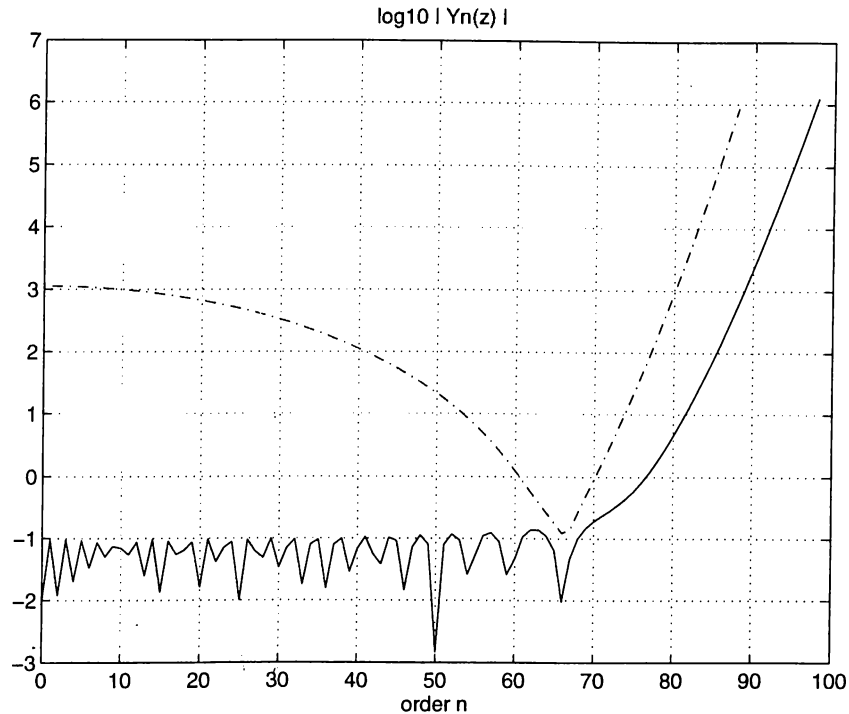
Figure 3.2: $|Y_n(z)|$, Argument: $z = 70 + 0i$ solid line, $z = 60 + 10i$ dash-dotted line

using forward recurrence for $n > r$ and backward recurrence for $n < r$ where $r$ is the value of $n$ to yield a minimum to $|Y_n(z)|$ for a given argument $z$.

## 3.2 Algorithm for $J_n(z)$

As explained above, backward recurrence is used to compute $J_n(z)$ from $J_q(z)$ and $J_{q+1}(z)$. The value of q must be sufficiently large for the starting value $J_{q+1}(z)$ to be practically zero (see Fig. 3.1). Let $B_n(z) = S.J_n(z)$ such that $B_{q+1}(z) = 0$ and $B_q(z) = 1$, the relative propagated error caused by the assumption that $B_{q+1}(z) = 0$ will diminish for smaller values of n. After repetitive use of (3.5) with decreasing $n$ starting from $q + 1$ and $q$, $J_n(z)$ is obtained by normalization of $B_n(z)$:

$$J_n(z) = \frac{B_n(z)}{S}. \tag{3.6}$$

When $Im[z] < 1$, the normalization constant S in (3.6) may be computed with the aid of the series [8,9]

13

$$1 \quad = \quad J_0(z) + 2 \sum_{k=1}^{\infty} J_{2k}(z)$$

$$S \quad = \quad S \, J_0(z) + 2 \sum_{k=1}^{\infty} S \, J_{2k}(z)$$

$$\approx \quad B_0(z) + 2 \sum_{k=1}^{q/2} B_{2k}(z). \tag{3.7}$$

The magnitude of any of the $B_n(z)$ functions is usually smaller and never much larger than S under the condition $Im[z] < 1$. This ensures that losses of significance caused by differences of large numbers in the summation will always be a minimum. When $Im[z] >> 1$, S will be magnitudes smaller than some of the terms in the summation, and serious losses of significance will occur. This is avoided by using the series [8,9],

$$S \cos(z) \quad = \quad S \, J_0(z) + 2 \sum_{k=1}^{\infty} (-1)^k \, S \, J_{2k}(z)$$

$$\approx \quad B_0(z) + 2 \sum_{k=1}^{q/2} B_{2k}(z), \tag{3.8}$$

when $Im[z] > 1$.

The following rule which is determined empirically by Du Toit [10], yield a minimum value for q (the starting point for backward recurrence) with high accuracy for real z, and for $M \leq |z|$ (where M is the maximum-required Bessel-function order) when double precision is required (double precision is used in both the radome and the slab calculations in this thesis):

$$q_{min} \approx \begin{cases} |z| + 10.26|z|^{0.341015} + 1.8, & |z| \leq 25 \\ |z| + 6.6362|z|^{0.342481} + 0.4, & |z| > 25. \end{cases} \tag{3.9}$$

## 3.3  Algorithm for $Y_n(z)$

As discussed before, when z is real the magnitude of $Y_n(z)$ is approximately constant for $n < |z|$ so higher orders may be computed from $Y_0(z)$ and $Y_1(z)$ using forward recurrence. Neumann's expansion is used for accurate computation of $Y_0(z)$ and $Y_1(z)$,

$$Y_0(z) = \frac{2}{\pi}[\ln(z/2) + \tau J_0(z) - 2\sum_{k=1}^{\infty}(-1)^k \frac{J_{2k}(z)}{k}], \qquad (3.10)$$

$$Y_1(z) = \frac{2}{\pi}[\ln(z/2) + \tau - 1 J_1(z) - \frac{J_0(z)}{z} - \sum_{k=1}^{\infty}(-1)^k \frac{(2k+1)J_{2k+1}(z)}{k(k+1)}]. \quad (3.11)$$

Only the significant $J_n(z)$ functions (until order $n = q$) are needed and the series are truncated at $n = q$.

When $z$ is complex, $Y_n(z)$ may be calculated for all $n$ from $Y_r(z)$ and $Y_{r+1}(z)$ using backward and forward recurrence.

After some experimentation it may be inferred that $|Y_r(z)|$ is at a minimum for a given complex argument when $r = [|z| + |Im(z)|/2]$ (this can be verified in Fig. 3.2). More precisely, a minimum occurs when [8]

$$Im(\frac{z}{r}\sin[\cos^{-1}(\frac{r}{z})]) = Im[\cos^{-1}(\frac{r}{z})]. \qquad (3.12)$$

This relation is tried using the Reguli Falsi numerical method to obtain r but it is seen that the approximate value $r = [|z| + |Im(z)|/2]$ gives quite reasonable values for r.

$Y_r(z)$ and $Y_{r+1}(z)$ are determined from $Y_0(z)$, $Y_1(z)$ and the $J_n(z)$ values as follows:

With the expansion of the recurrence relation (3.5), $Y_0(z)$, $Y_1(z)$ or $J_0(z)$, $J_1(z)$ can be written in terms of $Y_r(z)$, $Y_{r+1}(z)$ or $J_r(z)$, $J_{r+1}(z)$ as

$$B_0(z) = p_{11}B_r(z) + p_{12}B_{r+1}(z), \qquad (3.13)$$

$$B_1(z) = p_{21}B_r(z) + p_{22}B_{r+1}(z). \qquad (3.14)$$

By the Wronskian,

$$J_{n+1}(z)Y_n(z) - J_n Y_{n+1}(z) = \frac{2}{\pi z}, \qquad (3.15)$$

it is known that the determinant

$$\begin{vmatrix} p_{11} & p_{12} \\ p_{21} & p_{22} \end{vmatrix} \qquad (3.16)$$

is always equal to unity and it is used as a check in the codes.

15

Using known Bessel function values,

$$p_{11} = \frac{B_0}{B_r}, \tag{3.17}$$

$$p_{21} = \frac{B_1}{B_r}, \tag{3.18}$$

$$p_{12} = \frac{J_0(z) - p_{11}J_r(z)}{J_{r+1}(z)}, \tag{3.19}$$

$$p_{22} = \frac{J_1(z) - p_{21}J_r(z)}{J_{r+1}(z)}, \tag{3.20}$$

where $B_n(z)$ values are obtained for $n < r$ by backward recurrence starting from $B_{r+1}(z) = 0$ and $B_r(z) = 1$.

Hence the solution to (3.13) and (3.14) is

$$B_r(z) = -p_{12}B_1(z) + p_{22}B_0(z), \tag{3.21}$$

$$B_{r+1}(z) = p_{11}B_1(z) + p_{21}B_0(z). \tag{3.22}$$

Unfortunately, (3.21) and (3.22) cannot be used numerically when $Im[z]$ is large, because the terms on the right may be magnitudes larger than those on the left side of the equations, causing serious truncation errors. However, substition of (3.21) and (3.22) into (3.15) yield

$$Y_r(z) = \frac{1}{J_0(z)}[J_r(z)Y_0(z) + \frac{2p_{12}}{\pi z}], \tag{3.23}$$

$$Y_{r+1}(z) = \frac{1}{J_0(z)}[J_{r+1}(z)Y_0(z) + \frac{2p_{11}}{\pi z}]. \tag{3.24}$$

So, with $r$, $Y_r(z)$ and $Y_{r+1}(z)$, $Y_n(z)$ is produced by backward recurrence for $n < r$ and forward recurrence for $n > r$.

## 3.4  The Accuracy of the Algorithms

The accuracy of the algorithms were also tested by examining the numerical error in the Wronskian

$$error = J_{n+1}(z)Y_n(z) - J_n(z)Y_{n+1}(z) - \frac{2}{\pi z}. \tag{3.25}$$
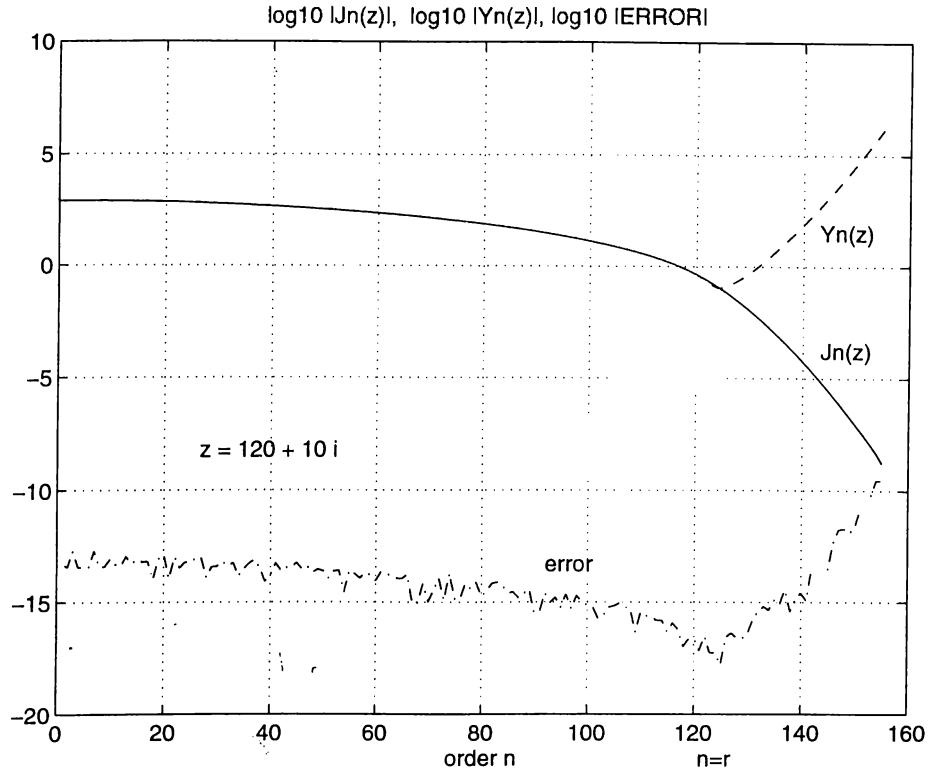
Figure 3.3: $|Relative\,Error|$

For illustration, this error is divided by $|J_{n+1}(z)| + |J_n(z)|$,

$$|\epsilon| = \frac{|J_{n+1}(z)Y_n(z) - J_n(z)Y_{n+1}(z) - \frac{2}{\pi z}|}{|J_{n+1}(z)| + |J_n(z)|} \quad . \tag{3.26}$$

The relative error $|\epsilon|$ is representative in all four functions involved.

The result follows when it is assumed that the relative errors in all four functions involved have the same amplitude, but are uncorrelated. This error $|\epsilon|$, $J_n(z)$ and $Y_n(z)$ for $z = 120 + 10i$ are depicted in Figure 3.3 . The relative error is in the order of $10^{-15}$, $10^{-16}$ which compares favorably with the double precision used in the codes.

# Chapter 4

# THE FAR FIELDS OF THE DIELECTRIC SLAB

## 4.1    Introduction

In this chapter, the far field radiation of real and complex line sources in the presence of a dielectric slab of infinite extent is investigated. The geometry of the problem is given in Figure 4.1 .

The fields of the unit line source located at the origin and radiating in free space satisfy the scalar wave equation [11],

$$[\frac{\partial^2}{\partial x^2} + \frac{\partial^2}{\partial y^2} + k_0^2]\Phi(x,y) = -\delta(x)\delta(y) \tag{4.1}$$

where $\Phi$ is the z-component of the electric or magnetic field depending on the nature of the source.

Because of the cylindrical symmetry, the equation above can be solved most conveniently in cylindrical coordinates,

$$[\frac{\partial^2}{\partial \rho^2} + \frac{1}{\rho}\frac{\partial^2}{\partial \rho} + k_0^2]\Phi(\rho) = -\delta(\rho). \tag{4.2}$$

Outside the source region, the right-hand side of (4.2) is zero and we have the Bessel's equation of zeroth order. In order to have an outgoing-wave solution that satisfies the radiation condition, the Hankel function of the first kind is chosen for $\Phi(\rho)$ with $e^{-iwt}$ time dependence. In other words,

$$\Phi(\rho) = C\, H_0^{(1)}(k_0\rho) \sim C\sqrt{\frac{2}{i\pi k_0\rho}}e^{ik_0\rho}, \quad k_0\rho \to \infty. \tag{4.3}$$

By matching the singularity of the Hankel function at $\rho = 0$ to the line source, one has

$$\Phi(\rho) = \frac{i}{4}H_0^{(1)}(k_0\rho)\ . \tag{4.4}$$

The application of the boundary conditions on the slab surfaces are easier to apply in cartesian coordinates. For this purpose, another solution including the Fourier transform technique is investigated. Assuming that the Fourier transform of $\Phi(x,y)$ exists, $\Phi(x,y)$ is expressible as a Fourier inverse transform integral,

$$\Phi(x,y) = \frac{1}{2\pi}\int_{-\infty}^{\infty}dk_x e^{ik_x x}\check{\Phi}(k_x,y). \tag{4.5}$$

Substituting (4.5) into (4.1) and using the fact that,

$$\delta(x) = \frac{1}{2\pi}\int_{-\infty}^{\infty}dk_x e^{ik_x x}, \tag{4.6}$$

it is obtained that,

$$\frac{1}{2\pi}\int_{-\infty}^{\infty}dk_x e^{ik_x x}[\frac{\partial^2}{\partial y^2} + k_0^2 - k_x^2]\check{\Phi}(k_x,y) = -\frac{1}{2\pi}\int_{-\infty}^{\infty}dk_x e^{ik_x x}\delta(y). \tag{4.7}$$

Since (4.7) is satisfied for all x, we must have

$$[\frac{\partial^2}{\partial y^2} + k_y^2]\check{\Phi}(k_x,y) = -\delta(y) \tag{4.8}$$

where $k_y^2 = k_0^2 - k_x^2$.

A particular solution to (4.8) is

$$\tilde{\Phi}_p = v_1(y)\ e^{ik_y y} + v_2(y)\ e^{-ik_y y}. \tag{4.9}$$

Substituting $\tilde{\Phi}_p$ in (4.8) one gets

$$i\ k_y\ v_1'(y)\ e^{ik_y y} - i\ k_y\ v_2'(y)\ e^{-ik_y y} = -\delta(y). \tag{4.10}$$

Also, imposing the condition [14]

$$v_1'(y)e^{ik_y y} + v_2'(y)e^{-ik_y y} = 0, \tag{4.11}$$

one solves for $v_1'(y)$ from the above set of equations and by integrating, it is found that $v_1(y) = \frac{i}{2k_y}$. Ignoring the physically unnecessary incoming-wave part, ie $v_2(y)$, the solution is obtained as

$$\tilde{\Phi}(k_x, y) = \frac{i\ e^{ik_y\ |y|}}{2k_y}. \tag{4.12}$$

Here, the radiation condition is satisfied by considering the outgoing-wave solution. Hence (4.5) becomes

$$\Phi(x, y) = \frac{i}{4\pi} \int_{-\infty}^{\infty} dk_x\ \frac{e^{ik_x\ x + ik_y\ |y|}}{k_y}. \tag{4.13}$$

By the uniqueness of the solution to the partial differential equation (4.1), (4.13) must also be equal to (4.4) since both of them satisfy (4.1). Hence, the spectral representation of the line source for the free space is obtained,

$$H_0^{(1)} = \frac{1}{\pi} \int_{-\infty}^{\infty} dk_x\ \frac{e^{ik_x\ x + ik_y\ |y|}}{k_y}\ . \tag{4.14}$$

This expression yields the plane wave expansion of the cylindrical wave of $H_0^{(1)}$.
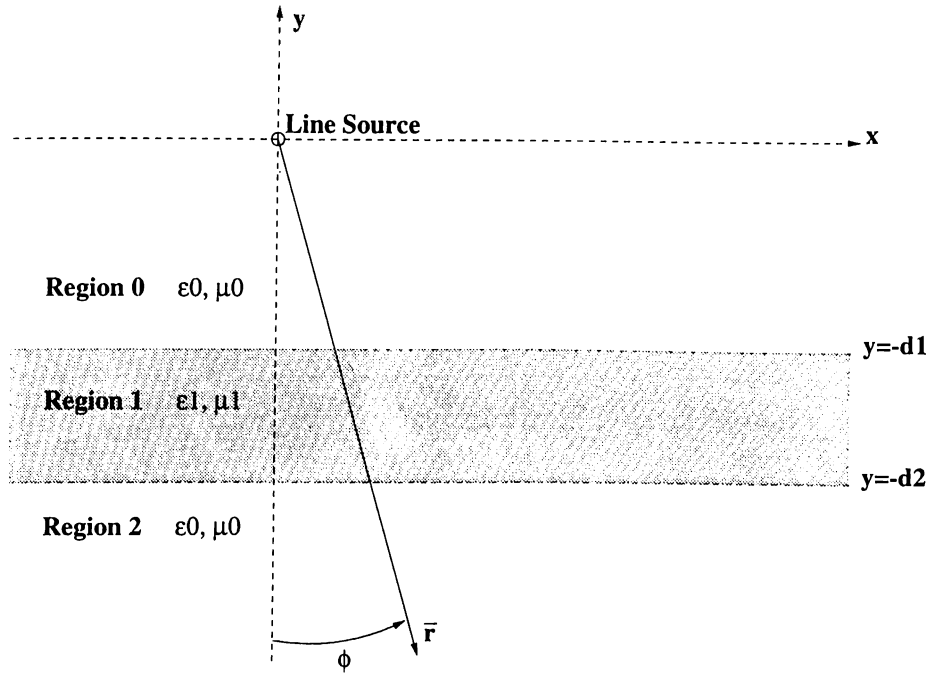
Figure 4.1: Slab Geometry ($\mu_0 = \mu_1$ is taken for simplicity).

Modifying (4.14) for the geometry provided (Fig. 4.1), the far zone transmitted field in Region 2 can be written as

$$U_z(\rho) = \frac{1}{\pi} \int_{-\infty}^{\infty} dk_x \; \check{T}(k_x) \; \frac{e^{ik_x\,x - ik_y\,|y|}}{k_y}, \tag{4.15}$$

where $\check{T}(k_x)$ is the transmission coefficient [12] for plane waves with the additional phase factor gained during the propagation through the dielectric slab. As seen from Fig. 4.1 $y$ takes negative values in Region 2. The integral in (4.15) is also known as Sommerfeld integral. The expression for $\check{T}(k_x)$ is given as:

$$\check{T}(k_x) = \frac{4\; e^{i(k_{1y} - k_{0y})(d_2 - d_1)}}{(1 + p_{01})(1 + p_{12})(1 + R_{01}R_{12}\; e^{i\,2\,k_{1y}\,(d_2 - d_1)})}. \tag{4.16}$$

where the parameters are as follows:

$$p_{01} = \frac{1}{p_{10}} = \frac{\mu_0 k_{1y}}{\mu_1 k_{0y}}, \left.\begin{array}{r}\\ \\ \end{array}\right\} \; For \; the \; TE \; case \qquad (4.17)$$
$$p_{12} = \frac{1}{p_{21}} = \frac{\mu_1 k_{2y}}{\mu_2 k_{1y}} = \frac{\mu_1 k_{0y}}{\mu_0 k_{1y}},$$

$$p_{01} = \frac{1}{p_{10}} = \frac{\epsilon_0 k_{1y}}{\epsilon_1 k_{0y}}, \left.\begin{array}{r}\\ \\ \end{array}\right\} \; For \; the \; TM \; case \qquad (4.18)$$
$$p_{12} = \frac{1}{p_{21}} = \frac{\epsilon_1 k_{2y}}{\epsilon_2 k_{1y}} = \frac{\epsilon_1 k_{0y}}{\epsilon_0 k_{1y}},$$

$$R_{01} = -R_{10} = \frac{p_{10}-1}{1+p_{10}}, \left.\begin{array}{r}\\ \\ \end{array}\right\} \; For \; both \; the \; TE \; and \; TM \; cases \qquad (4.19)$$
$$R_{12} = -R_{21} = \frac{p_{21}-1}{1+p_{21}},$$

$$k_x^2 + k_{0y}^2 = k_0^2, \qquad (4.20)$$
$$k_x^2 + k_{1y}^2 = k_1^2. \qquad (4.21)$$

The right hand side of (4.15) can be interpreted as an integral summation of plane waves propagating through the slab in different directions into Region 2 including evanescent waves. Furthermore, these plane waves satisfy the dispersion relations (4.20, 4.21). Hence (4.15) is the plane wave expansion of a cylindrical wave passing through the dielectric slab. Due to (4.20) and (4.21), $k_{0y}$ and $k_{1y}$ can be complex numbers. In order to satisfy the radiation condition of having only outgoing waves in the integrand, it must be ensured that $Im[k_y] > 0, \quad Re[k_y] > 0$.

In addition, the branch point singularities in (4.15) (at $k_{0y} = \sqrt{k_0^2 - k_x^2} = 0$, $k_x = \pm k_o$) should be avoided by the path of integration as shown in Figure 4.2(a). To carry out numerical integration, the path in Figure 4.2(b) is more suitable. If a small loss is assumed by adding a small imaginary part in $\epsilon_r$, the wave field becomes absolutely integrable and the integral becomes well-behaved.

Three methods of numerical integration of the Sommerfeld integral were tested. For all three, $x$ and $y$ were kept large, so that the observation point was in far field. But this made the integrand oscillate rapidly and the integration hard to be calculated. The adaptive recursive Simpson's rule and Newton Cotes panel 8 rule didn't give satisfactory results. For a dependable integral algorithm, Filon Quadrature Method [13] is tried for the rewritten form of (4.15):

$$H(\rho) = \frac{2}{\pi} \int_0^\infty dk_x \, \cos(k_x x) \tilde{T}(k_x) \frac{e^{-i k_y y}}{k_y}. \qquad (4.22)$$
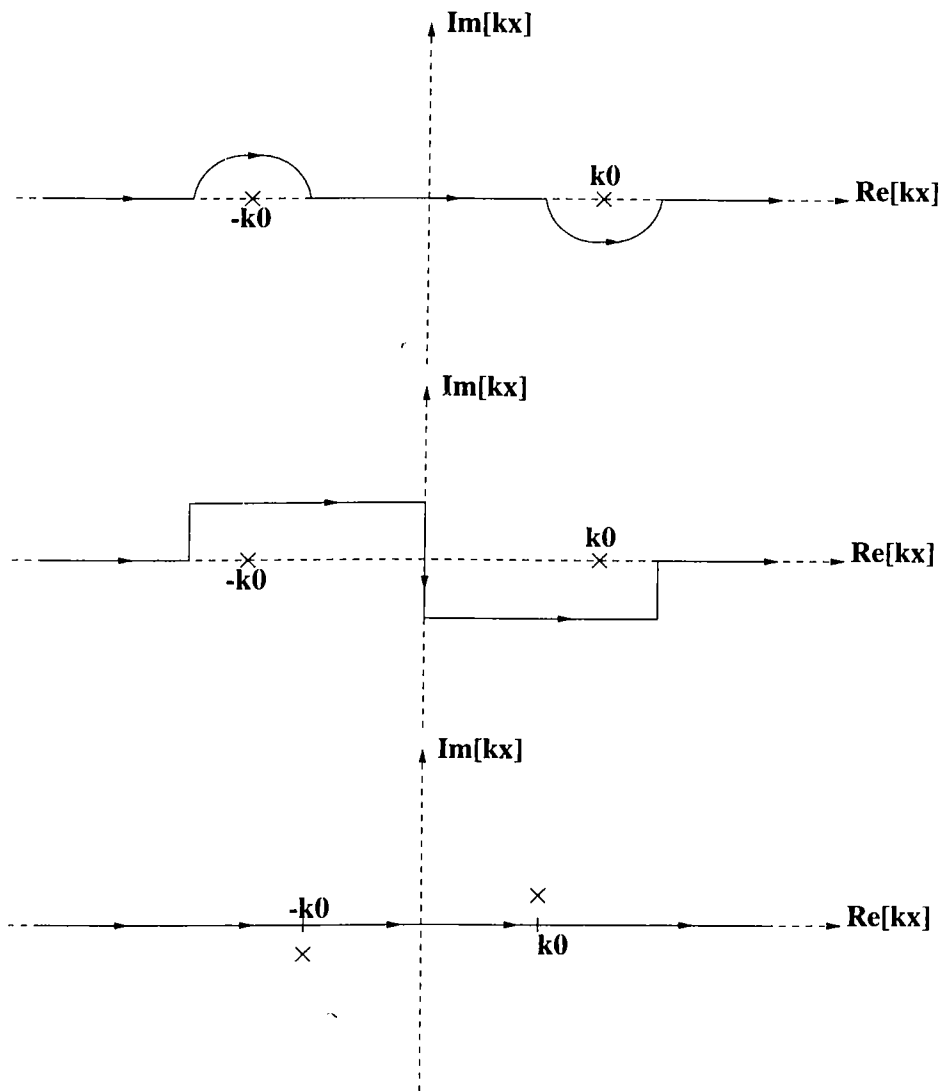
22

Figure 4.2: Different Paths of Sommerfeld Integration

In this algorithm, the integral $\int_a^b dx \cos(k\,x)\,f(x)$ is calculated by using the Filon cosine formula

$$\int_a^b dx \cos(k\,x)f(x) = h[\alpha(f_n \sin k\,x_n - f_0 \sin k\,x_0) + \beta\,C_e + \gamma\,C_o], \quad (4.23)$$

with the interval [a,b] and $f_n$ is the value of the function at $x_n$. The following abbreviations with the cosine and sine sums complete the algorithm:

$$\theta = k\,h = \frac{k(b-a)}{n}, \quad (4.24)$$

$$\alpha(\theta) = \frac{\theta^2 + 0.5\theta \sin 2\theta - 2\sin^2 \theta}{\theta^3}, \quad (4.25)$$

$$\beta(\theta) = 2\,\frac{\theta(1 + \cos^2 \theta) - \sin 2\theta}{\theta^3}, \quad (4.26)$$

$$\gamma(\theta) = 4\,\frac{\sin \theta - \theta \cos \theta}{\theta^3}, \quad (4.27)$$

$$C_e = \frac{1}{2}f_0\,x_o + f_2 \cos k\,x_2 + \ldots + f_{n-2} \cos k\,x_{n-2} + \frac{1}{2}f_n \cos k\,x_n, \quad (4.28)$$

$$C_o = \frac{1}{2}f_0\,x_0 + f_3 \cos k\,x_3 + \ldots + f_{n-1} \cos k\,x_{n-1}, \quad (4.29)$$

where $C_e$ involves only ordinates with even subscripts and $C_o$ only those with odd subscripts.

Filon's method has given dependable results when $|y|$ and $\phi$ (the angle of the observation point, see Fig 4.1) are not large, that is when the observation point is located not far from the slab along the normal.

However, fields are needed to be found for the far field ($r \rightarrow \infty$) and an asymptotic approach would give much more dependable results than any numerical solution would. So the Sommerfeld integral in (4.15) is treated in analytical terms.

## 4.2 Stationary Phase Solution For The Real Line Source

Rewriting the Sommerfeld integral for real line source when $x = \rho \sin \phi$, $y = -\rho \cos \phi$ ($\vec{r} = x\,\vec{x} + y\,\vec{y}$ and $\rho \rightarrow \infty$), one has

$$U(\rho) = \frac{1}{\pi} \int_{-\infty}^{\infty} dk_x \; \tilde{T}(k_x) \frac{e^{ik_x \, x - ik_y \, y}}{k_y} = \int_{-\infty}^{\infty} dk_x \; F(k_x) \; e^{i \, \Phi(k_x)}. \qquad (4.30)$$

The highly oscillating and the stationary parts of the integrand are $e^{i\Phi(k_x)}$ and $F(k_x)$, respectively, where

$$F(k_x) = \frac{\tilde{T}(k_x)}{k_y}, \qquad (4.31)$$

$$\Phi(k_x) = k_x \, x - k_y \, y = \rho(k_x \sin\phi + \sqrt{k_0^2 - k_x^2} \cos\phi), \qquad (4.32)$$

$$\Phi'(k_x) = \rho \sin\phi - k_x \frac{\rho \cos\phi}{\sqrt{k_0^2 - k_x^2}}, \qquad (4.33)$$

$$\Phi''(k_x) = -\rho \cos\phi \; \frac{k_0^2}{[k_0^2 - k_x^2]^{3/2}}. \qquad (4.34)$$

The stationary phase point is obtained by setting

$$\Phi'(k_{x_s}) = 0 \;\; \Rightarrow \;\; k_{x_s} = \pm k_0 \sin\phi. \qquad (4.35)$$

Using the fact that,

$$U(\rho) = \int_{-\infty}^{\infty} dk_x \; F(k_x) \; e^{i\Phi(k_x)} \sim F(k_{x_s}) \sqrt{\frac{2\pi}{|\Phi''(k_{x_s})|}} e^{i[\Phi(k_{x_s}) + \frac{\pi}{4} sgn \Phi''(k_{x_s})]}, \quad (4.36)$$

and ignoring the stationary phase point at $k_x = -k_0 \sin\phi$ (since this corresponds to the incoming waves) the real line source solution is found to be

$$U(\rho) \sim \sqrt{\frac{2}{\pi k_o \rho}} \; e^{ik_o \rho} \; e^{-i\frac{\pi}{4}} \; \tilde{T}(k_0 \; \sin\phi), \qquad (4.37)$$

where the large argument expansion of the first kind zeroth order Hankel function can be recognized,

$$H_0^{(1)} \sim \sqrt{\frac{2}{\pi k_o \rho}} e^{ik_0 \rho} e^{-i\frac{\pi}{4}} \quad (k_0 \rho \to \infty). \qquad (4.38)$$
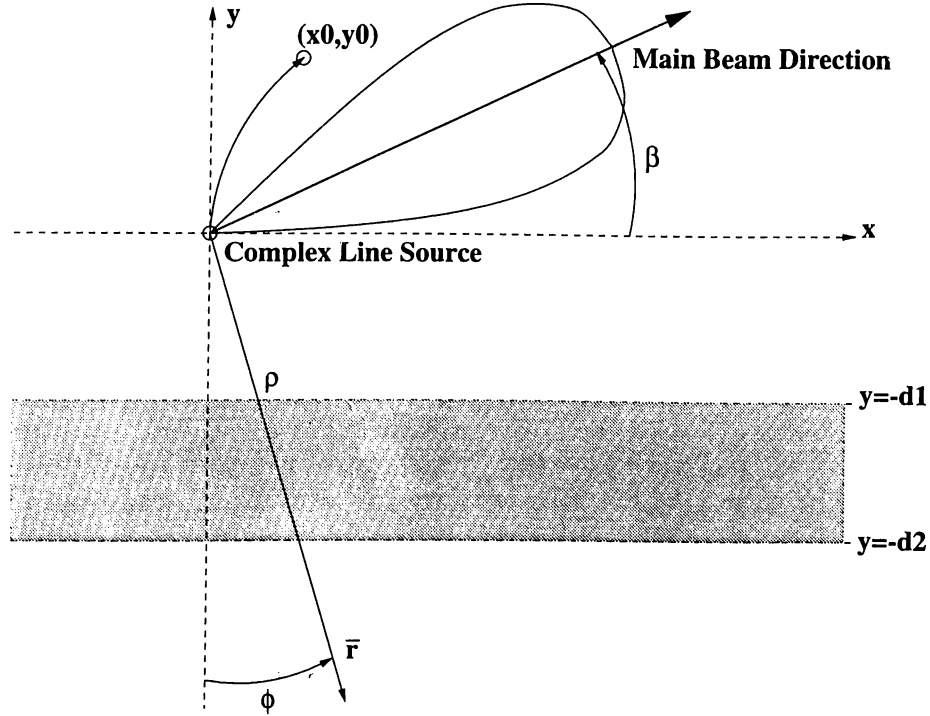
25

Figure 4.3: The Complex Line Source at the Slab Geometry. Here, $\beta$ is the angle of main beam direction, $\vec{r_s}$ is the physical location vector, and 2b is the aperture width of the complex line source ($\vec{r_0}$, $b$ not shown).

## 4.3 Stationary Phase Solution For Complex Line Source

In this case, the line source is located at a complex position vector $\vec{r_s}$:

$$\vec{r_s} = \vec{r_0} + i\vec{b} = \vec{r_0} + ib(\cos\beta\hat{x} + \sin\beta\hat{y}). \tag{4.39}$$

The vector $\vec{r_s}$ can also be represented by its magnitude and angle,

$$r_s = \sqrt{r_0^2 - b^2 + 2ibr_0\cos\beta}, \tag{4.40}$$

$$\theta_s = \cos^{-1}\left(\frac{r_0 + ib\cos\beta}{r_s}\right). \tag{4.41}$$

The real part of $\vec{r_s}$ corresponds to the source location at the origin, $r_0 = 0$, so

$$\vec{r_s} = (\hat{x}\cos\beta + \hat{y}\sin\beta)ib, \tag{4.42}$$

26

$$r_s = ib, \tag{4.43}$$

$$\theta_s = \cos^{-1}\left(\frac{ib\cos\beta}{r_s}\right) = \beta. \tag{4.44}$$

To obtain the far field expression for the complex line source radiating through the lossless ($Im[\epsilon_r] = 0$), infinite, dielectric slab, a shift in the coordinates of the real line source will be applied to (4.15). First it is assumed that the real line source is located at $(x_0, y_0)$ instead of the origin,

$$U(\rho) = \frac{1}{\pi} \int_{-\infty}^{\infty} dk_x \; \tilde{T}(k_x) \; e^{ik_x(x-x_0)} \; e^{ik_y\, y_0} \; \frac{e^{-ik_y\, y}}{k_y}. \tag{4.45}$$

Next, $\vec{r_s} = \hat{x}ib\cos\beta + \hat{y}ib\sin\beta$ is substituted instead of $(x_0, y_0)$ and the following expression is obtained:

$$U(\rho) = \frac{1}{\pi} \int_{-\infty}^{\infty} dk_x \; \tilde{T}(k_x) \; e^{ik_x(x-ib\cos\beta)} \; e^{ik_y(ib\sin\beta)} \; \frac{e^{-ik_y\, y}}{k_y}. \tag{4.46}$$

Choosing the stationary and rapidly oscillating parts of the integrand and applying the stationary phase approximation procedure,

$$F(k_x) = \frac{1}{\pi}\tilde{T}(k_x) \; e^{b\, k_x\, \cos\beta} \; \frac{e^{-k_y\, b\, \sin\beta}}{k_y}, \tag{4.47}$$

$x = \rho\sin\phi, \; = -\rho\cos\phi,$

$$\Phi(k_x) =_x \sin\phi + \sqrt{k_0^2 - k_x^2}\rho\cos\phi, \tag{4.48}$$

the same expressions for the complex line source are obtained for $\Phi'(k_x)$, $\Phi''(k_x)$ and the stationary phase point $k_{x_s}$ as in (4.33), (4.34) and (4.35) for the real source.

Using (4.36) and ignoring $k_{x_s} = -k_0\sin\phi$ for the same reason as for the real line source, the following far field expression is obtained:

$$U_z(\rho) \sim \sqrt{\frac{2}{\pi k_0\rho}} \; e^{ik_0\rho} \; e^{-i\frac{\pi}{4}} \; \tilde{T}(k_0\,\sin\phi) \; e^{b\, k_0\,(\sin\phi\cos\beta-\cos\phi\sin\beta)}. \tag{4.49}$$

In (4.49) the large argument expansion of the first kind zeroth order Hankel function $H_0^{(1)}(k_0\rho)$ can be recognized, see (4.38).
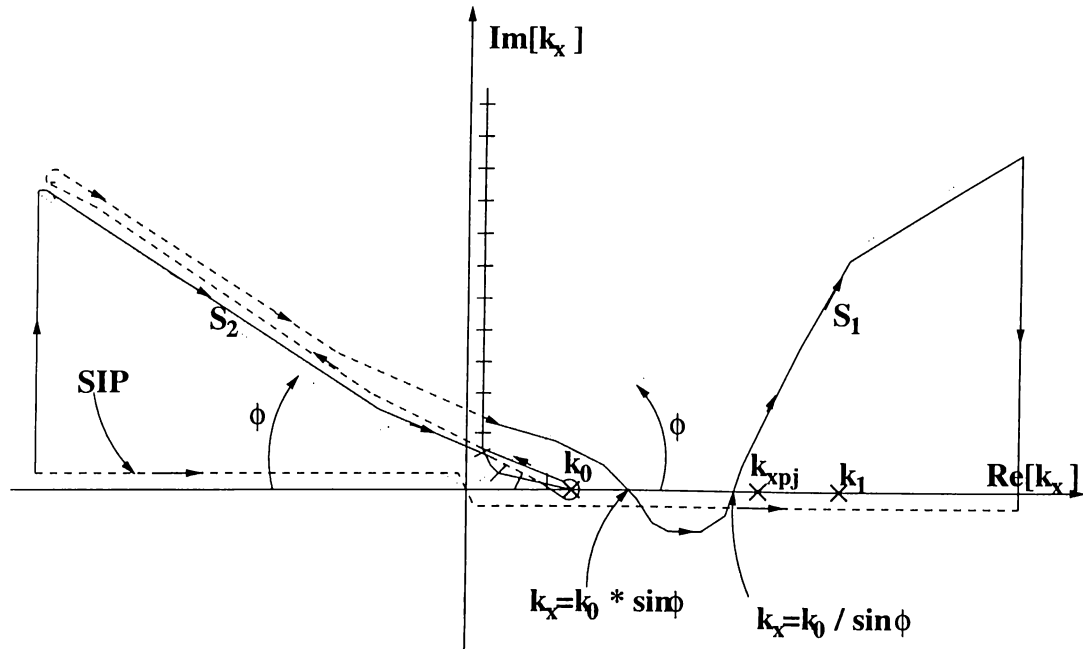
27

Figure 4.4: Branch points ($k_0$ and $k_1$), steepest-descent paths (constant-phase paths) passing through the saddle point (stationary phase point $k_{x_s}$) and the Sommerfeld integration path (SIP)

## 4.4 Contribution Of Surface Wave Poles

The integrands of the Sommerfeld integrals have singularities on the complex $k_\rho$ plane or $k_x$ plane in 2D case. The nature of these singularities affect the results of asymptotic expansions and uniform asymptotic expansions. They also affect the definition of the integration paths if the Sommerfeld integrals are to be evaluated numerically as described in section 4.1 .

There are two basic types of singularities - the pole singularities and the branch-point singularities. The pole singularities correspond to guided modes in the layered medium. The branch points correspond to radiation modes. These radiation modes form a continuum of modes. In addition, for the layered medium, the branch points are only associated with the outermost regions, as shown in [11, subsection 2.7.1].

The branch points in the integrand (4.46) $k_y = \sqrt{k_0^2 - k_x^2}$, the saddle point and integration paths are shown in Figure 4.4 . In our problem, with reference to Figure 4.1, the outermost regions (the regions 0 and 2) are free space, so the wavenumbers in these regions coincide $k_2 = k_0$. So only $k_0$ is shown in Figure 4.4 . SIP is the conventional Sommerfeld integration path which would be modified as needed. SIP avoids the branch point singularities as also described

28

for Figure 4.2 . The constant-phase path or the steepest-descent path that passes through the saddle point $k_{x_s} = k_0 \sin \phi$ is shown as $S_1$. Furthermore, the constant-phase path around the branch point $k_0$ is $S_2$. By virtue of Jordan's lemma and Cauchy's theorem, we can deform the contour from the Sommerfeld integration path (SIP) to the paths $S_2$ and $S_1$. The region enclosed by $S_2$, $S_1$ and SIP is analytic except for the possible occurrence of pole singularities. Moreover, the contribution from the two vertical paths vanishes due to Jordan's lemma when they tend to infinity. The stationary phase solution is the same as that one would have obtained by finding the leading-order saddle-point contribution.

When the integration path is deformed from the original path of integration to the constant-phase path passing through the saddle point at $k_{x_s} = k_0 \sin \phi$, a $k_2$ (wavenumber in Region 2) branch-point contribution should be included if $k_0 \sin \phi > k_2$. But, since Region 2 is formed of free space ($k_2 = k_0$) and $\phi < 90^\circ$ is of interest, no branch point contribution is needed (no lateral waves which correspond to branch point contributions). Furthermore, by noting the point where the steepest descent path crosses the real axis, the guided-mode contribution will be included if $k_0/\sin \phi < k_{x_{p_j}}$, the location of the j-th guided mode. Also, the guided-mode poles have to be such that $k_0 < k_{x_{p_j}} < k_1$ because a guided mode in medium 1 is evanescent both in media 0 and 2. So, the criteria to be used for selecting which poles to contribute is

$$\frac{k_0}{\sin \phi} < k_{x_{p_j}} < k_1. \tag{4.50}$$

The pole singularities of the integrand as a consequence of (4.16) have to be identified in order to find the complete field in Region 2. The poles of (4.16) are given by the equation

$$1 + R_{01} \, R_{12} \, e^{i2k_{1y}(d_2 - d_1)} = 0. \tag{4.51}$$

Physically, the above implies that a wave, after reflecting from the top and the bottom interfaces, together with a phase shift through the slab, should become in phase with itself again. This is precisely the guidance condition (sometimes referred to as the transverse resonance condition) for guided modes in a dielectric slab. Therefore, these poles in the complex $k_x$ plane are actually related to the guided modes of a dielectric slab. Moreover, since $k_{jy} = \sqrt{k_j^2 - k_x^2}$, equation (4.51) is just a function of $k_x$. Hence the roots of (4.51) can be solved numerically.

The number of guided-mode poles of a slab depends on the frequency and the thickness of the slab. For instance, there are a large number of guided-mode poles at high frequencies and a fewer number of poles at low frequencies. Moreover, the thicker the slab, the more guided-mode poles there are.

Since Region 2 is free space, $R_{12} = R_{10}$. Using the facts that $R_{10} = -R_{01}$ and $R_{01} = e^{i2\phi_{01}}$ where $\phi_{01}^{TE} = -\tan^{-1}(\frac{\mu_1 \alpha_{0y}}{\mu_0 k_{1y}})$ for TE waves (H polarization) and $\phi_{01}^{TM} = -\tan^{-1}(\frac{\epsilon_1 \alpha_{0y}}{\epsilon_0 k_{1y}})$ for TM waves (E polarization) are the phase shifts of the Fresnel reflection coefficients (also known as the Goos-Hänchen shifts) in (4.51), the transcendental equations are obtained:

$$
TE \begin{cases} \alpha_{0y} \frac{d}{2} = k_{1y} \frac{d}{2} \tan(k_{1y} \frac{d}{2}) & Even, \\ \alpha_{0y} \frac{d}{2} = -k_{1y} \frac{d}{2} \cot(k_{1y} \frac{d}{2}) & Odd, \end{cases} \tag{4.52}
$$

$$
TM \begin{cases} \alpha_{0y} \frac{d}{2} = \frac{\epsilon_0}{\epsilon_1} k_{1y} \frac{d}{2} \tan(k_{1y} \frac{d}{2}) & Even, \\ \alpha_{0y} \frac{d}{2} = -\frac{\epsilon_0}{\epsilon_1} k_{1y} \frac{d}{2} \cot(k_{1y} \frac{d}{2}) & Odd, \end{cases} \tag{4.53}
$$

where also $\alpha_{0y} = i k_{0y}$ and $d = d_2 - d_1$ abbreviations are used.

Additionally, combining the dispersion relations for both media,

$$
k_0^2 = k_x^2 - \alpha_{0y}^2, \quad Region\,0, \tag{4.54}
$$

$$
k_1^2 = k_x^2 + k_{1y}^2, \quad Region\,1, \tag{4.55}
$$

the needed second relation to be used with the transcendental equations is obtained:

$$
(k_{1y}d)^2 + (\alpha_{0y}d)^2 = (k_1^2 - k_0^2)d^2. \tag{4.56}
$$

The guidance condition can be plotted on a two-dimensional plane determined by $\alpha_{0y}d$ and $k_{1y}d$ [Figure 4.5] . The two sets of curves intersect and give rise to values of $\alpha_{0y}d$ and $k_{1y}d$, which in turn determine $k_{x_p}$.

Referring to (4.30) the contribution of the guided-mode poles to the far field of the real line source radiating through an infinite dielectric slab can be written as
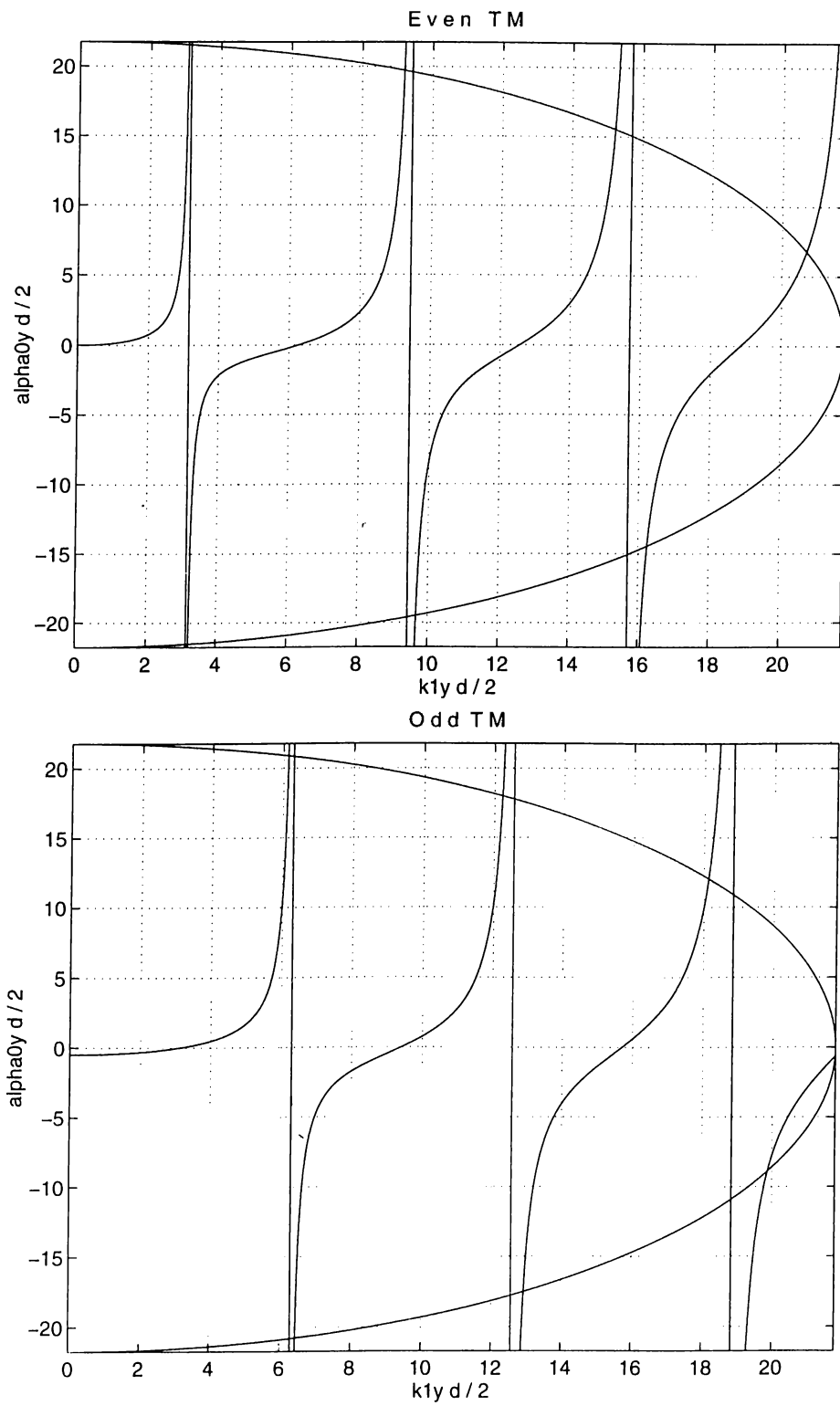
30

Figure 1.5: TM even and odd transcendental equations with combined dispersion relations at $d = 2\lambda$ thickness. Similar for the TE case.

$$U_z^{contribution} = \frac{1}{\pi} \sum_j \frac{e^{i\rho(k_x \sin\phi + k_y \cos\phi)}}{k_y}\Big|_{k_x = k_{x_{p_j}}} 2\pi i \; Res[\tilde{T}(k_{x_{p_j}})], \qquad (4.57)$$

where the poles are selected using the criteria (4.50) and
$$Res[\dot{T}(k_{x_{p_j}})] = \tilde{T}_{numerator}(k_{x_{p_j}})/\tilde{T}'_{denominator}(k_{x_{p_j}}).$$

Referring to (4.46), similarly, the pole contribution for the complex line source is

$$U_z^{contribution} = \frac{1}{\pi} \sum_j e^{k_x b \cos\beta - k_y b \sin\beta} \frac{e^{i\rho(k_x \sin\phi + k_y \cos\phi)}}{k_y}\Big|_{k_x = k_{x_{p_j}}} 2\pi i \; Res[\check{T}(k_{x_{p_j}})] \;.$$
$$(4.58)$$

# Chapter 5

# NUMERICAL RESULTS AND COMPARISONS

As stated in the introduction, the motivation for the comparison of the radome and slab fields is that as the far field in the main beam direction is concerned, radome of the larger radius approaches geometrically to an infinite dielectric slab. So the intuitive expectation should be the decrease of discrepancy between the far fields of the two models in the main beam direction as the radius of radome is increased. To do this comparison, the geometries and the fields should be arranged clearly and correctly. Also, the comparison criteria should be chosen properly.
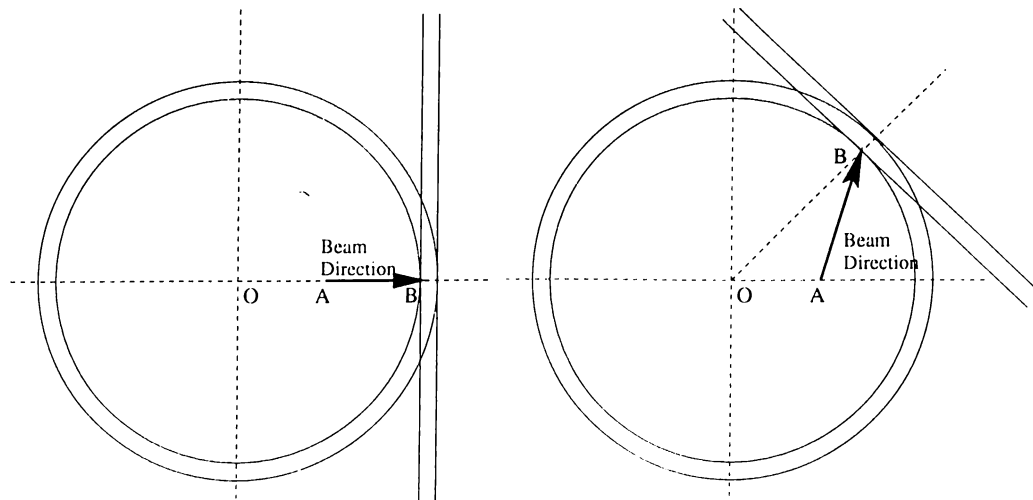


Figure 5.1: Dielectric slab and radome illuminated by a complex source at A. a) Normal Incidence, b) Inclined Beam

There are two conditions about the placement of the slab, when the beam

of the complex source is directed normally to the slab (Figure 5.1(a)) and when the beam is an inclined one with respect to the slab (Figure 5.1(b)). In both figures the complex line source is placed at point A and, in fact, normal incidence is only a special condition of the more general case of the inclined incidence. In principle, the infinite slab is placed as a tangent at the point where the main beam axis crosses the radome (point B in Figure 5.1). This is shown more clearly in Figure 5.2 and 5.3 where only the inner boundaries of the radome and the slab are shown.
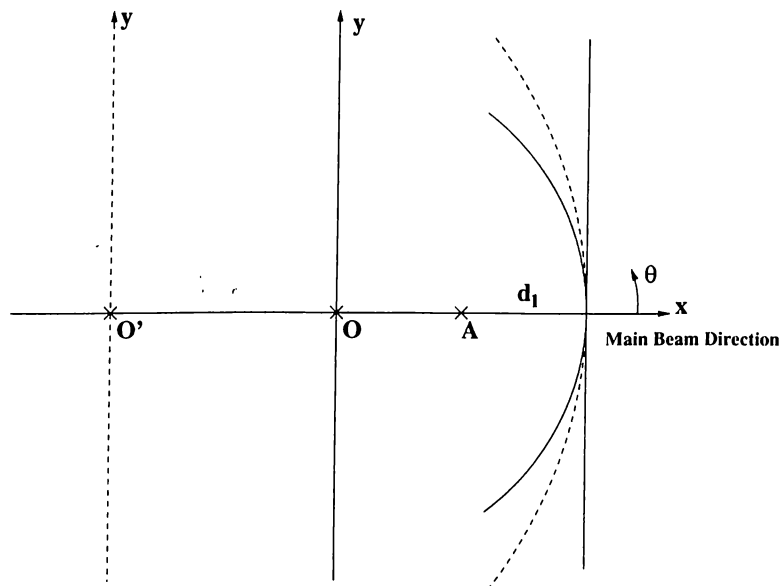


Figure 5.2: Geometry for the normal incidence

Initially, the case when the beam is directed along the x-axis (normal incidence) is considered. In Figure 5.2, the radome is centered at point O and the source is located at point A. If the radius of the radome is increased by keeping the tangent condition to the slab, the center of the radome has to be moved towards left (such as point O' as shown in Figure 5.2). It is expected that a better comparison is obtained for larger radome radius with the slab solution.

When the beam is an inclined one (see Figure 5.3), one should keep the slab parameters $d_1$ and $\beta_{Slab}$ constant as the radome geometry is changed. So the following relations are used to calculate the radome parameters $a$ and $\beta_{Radome}$ using fixed slab parameters:

$$\beta_{Radome} = \cot^{-1}[\frac{1}{\sin(\beta_{Slab})}(\cos(\beta_{Slab}) - \frac{e}{c})], \qquad (5.1)$$

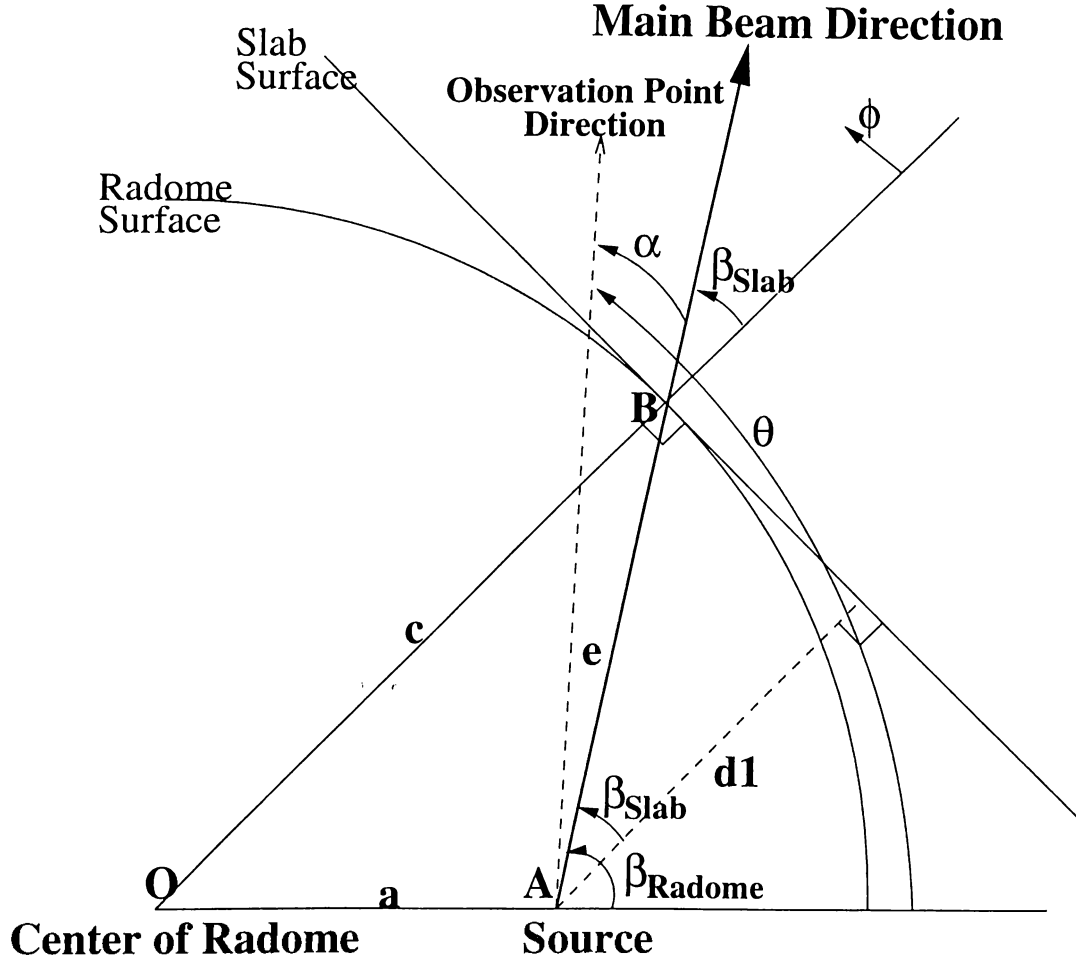$$a = c\frac{d_1}{\cos(\beta_{Slab})}, \qquad (5.2)$$

34

Figure 5.3: Geometry for the inclined beam

where $e = \frac{d_1}{\cos \beta_{Slab}}$.

It is noted that the phase centers of the radome and slab fields are at points O and A, respectively. So, for comparing the fields, the phases are represented with respect to the same point, ie. the center of the radome.

As a check, the free space radiation pattern is obtained when $\epsilon_r$ is set to 1 in the radome and slab codes (free space or empty radome and slab instead of dielectric) for both polarizations and compared with the source fields.

In Figures (5.4) through (5.19), the far fields of the complex sources ($b = 0.2\lambda$) radiating through dielectric ($\sqrt{\epsilon_r} = 2$) radome and slab are plotted when the thickness of the radome and the slab is $2\lambda$. We can denote the far fields as $U^r$ and $U^s$ for the radome and slab models, respectively. The plots consist of three parts: a) $|U^r|$ and $|U^s|$ as the magnitudes, b) $|U^r - U^s|$ as the field difference magnitude, c) $\angle U^r$ and $\angle U^s$ as the phases of the fields. In these plots, both polarizations and two values of inclination angle ($\beta_{Slab} = 0, 30^o$) are

presented. For inclined beam cases, the slab parameters $d_1 = 3\lambda$ and $\beta_{Slab} = 30^o$ are kept constant. The radome parameters $a$ and $\beta_{Radome}$ are calculated according to (5.1) and (5.2). For $\beta_{Slab} = 0^o$, $a = c - d_1$ and $\beta_{Radome} = 0^o$ are applied simply.

Rather than examining the field differences at specific angles, the average field differences spanning the region of interest (main beam) is more convenient. The extent of the span around the main beam direction is chosen to be $\pm 40^o$, which is wide enough to take the whole beam into account. The mean, $M$, and the mean square differences, $M^2$, represent an average within the spanning region with the relations

$$
M = \frac{\sum_{\alpha=-40^o}^{40^o} |U^r - U^s|}{N}, \qquad M^2 = \frac{\sum_{\alpha=-40^o}^{40^o} |U^r - U^s|^2}{N}, \qquad (5.3)
$$

where $N$ represents the number of samples in $-40^o \leq \alpha \leq 40^o$. As a meaningful interpretation of the plots provided, Tables 1-4 can be referred where the mean and the mean square differences in fields are calculated spanning $\pm 40^o$ around the main beam direction (the spanning angle $\alpha = \theta - \beta_{Radome}$, Figure 5.3).

The results obtained confirm the idea of improving the approximation of the radome by the slab when the radome radius is increased.

When the radome radius is not large, different waveguide and resonance properties of the dielectric slab and circular radome, point to quite clear differences in the far field patterns. The fields become different in phase when the spanning angle, $\alpha$, is non-zero, see Figures 5.4, 5.8, 5.12 and 5.16 . Also, the amplitude of the radome field is more oscillatory as compared to the slab far field. Finally, the field differences include the boresight error and peak-gain attenuation.

With the greater radius $c$, the differences decrease, see Tables 1-4. This is mainly due to the fact that the phase matching of the slab and radome fields is much better satisfied when $c$ is increased. One can see, however, some distinctions between $E$ and $H$ polarizations. The field difference appears to be a little greater in the $H$ case especially at large spanning angles $\alpha$. Also, the differences are greater for the inclined beams.

Notice that the conclusion on the radome and slab field convergence which follows from the results above, is actually a sort of "asymptotic" nature because some field differences still exist far from the main beam, even for large $c$. It could be the effect of the difference between the closed radome and the open

slab topologies resulting in different waveguide and resonance properties of these structures. The effect, however, is minor when the beam is narrow and directed normal to the slab.

The results obtained in this work, show the limitations for the approximation of the radome by the infinite dielectric slab in the far field around the main beam for the directed sources.

## 5.1 Frequency and Thickness Dependence

To understand how the radome and the slab affects the radiated fields, it is worthwhile to see what happens when the frequency and the thickness of the dielectric are changed. The far fields in the main beam direction as a function of frequency and wavelength are plotted in Figures 5.20, 5.22 for the radome and slab models respectively (the case of $E$ polarization, $\beta = 0$, $\phi = 0$). In these plots, the distorted effects of the closed radome model in addition to the similar behaviors of the fields are observed. The thicknesses of the radome and the slab are changed in Figures 5.21 and 5.23 . The periodicity of the far field as a function of thickness is observed, with the period of $\lambda_{diel}/2$, as expected, where $\lambda_{diel} = \lambda_0/\sqrt{\epsilon_r}$, $\epsilon_r = 4$ and $\lambda_0$ is the free space wavelength.

| Table 1, E Polarization, $\beta_{Slab} = 0$, $d_1 = 3\lambda$ | | | |
|---|---|---|---|
| Inner Radome Radius | Mean Error | Mean Square Error | Figure Number |
| $c = 5\lambda$ | 1.197953 | 0.055573 | Fig 5.4 |
| $c = 10\lambda$ | 0.899181 | 0.041840 | Fig 5.5 |
| $c = 20\lambda$ | 0.556542 | 0.025704 | Fig 5.6 |
| $c = 40\lambda$ | 0.323722 | 0.013925 | Fig 5.7 |

| Table 2, E Polarization, $\beta_{Slab} = 30$, $d_1 = 3\lambda$ | | | |
|---|---|---|---|
| Inner Radome Radius | Mean Error | Mean Square Error | Figure Number |
| $c = 5\lambda$ | 2.362785 | 0.108388 | Fig 5.8 |
| $c = 10\lambda$ | 1.823967 | 0.091400 | Fig 5.9 |
| $c = 20\lambda$ | 1.219008 | 0.066617 | Fig 5.10 |
| $c = 40\lambda$ | 0.744024 | 0.041387 | Fig 5.11 |

| Table 3, H Polarization, $\beta_{Slab} = 0$, $d_1 = 3\lambda$ | | | |
|---|---|---|---|
| Inner Radome Radius | Mean Error | Mean Square Error | Figure Number |
| $c = 5\lambda$ | 1.10704 | 0.050534 | Fig 5.12 |
| $c = 10\lambda$ | 0.88236 | 0.037627 | Fig 5.13 |
| $c = 20\lambda$ | 0.66267 | 0.026212 | Fig 5.14 |
| $c = 40\lambda$ | 0.54899 | 0.021671 | Fig 5.15 |

| Table 4, H Polarization, $\beta_{Slab} = 30$, $d_1 = 3\lambda$ | | | |
|---|---|---|---|
| Inner Radome Radius | Mean Error | Mean Square Error | Figure Number |
| $c = 5\lambda$ | 2.021541 | 0.090874 | Fig 5.16 |
| $c = 10\lambda$ | 1.710943 | 0.078746 | Fig 5.17 |
| $c = 20\lambda$ | 1.177634 | 0.056916 | Fig 5.18 |
| $c = 40\lambda$ | 0.782151 | 0.034336 | Fig 5.19 |
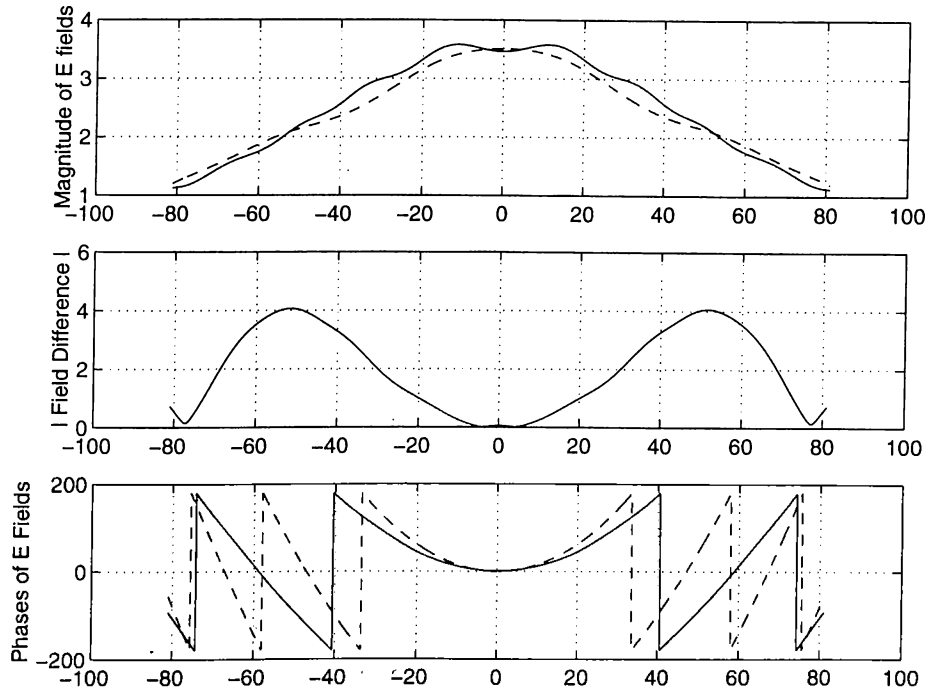
Figure 5.4: Far Fields of Radome (solid curve) and Slab (dashed curve) as functions of $\theta$ (E Polarization, Normal Incidence, $c = 5\lambda$, $\beta_{Radome} = \beta_{Slab} = 0°$, $\alpha = \theta - \beta_{Radome}$)
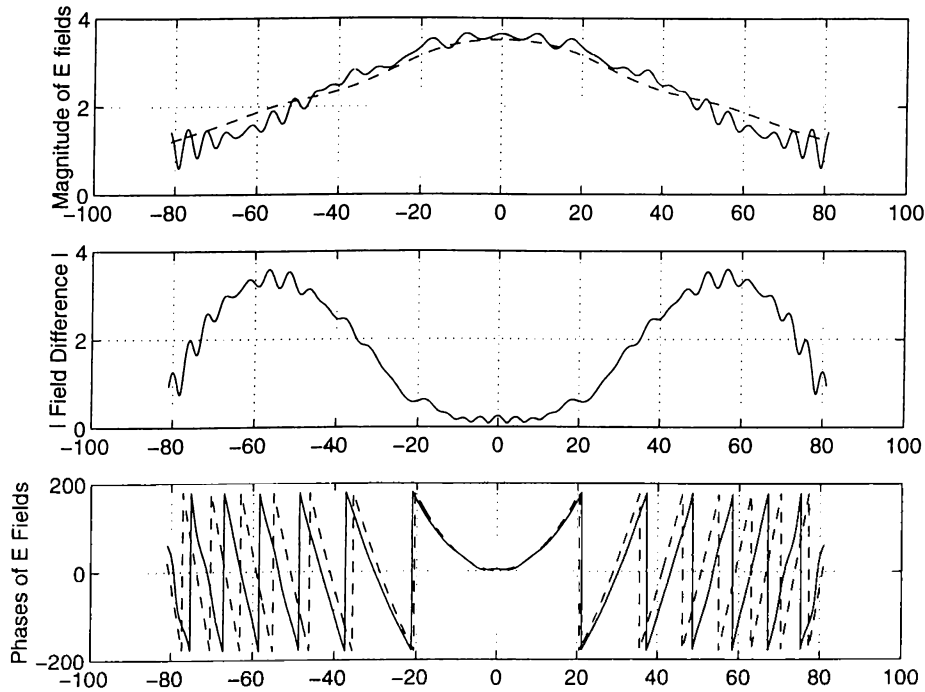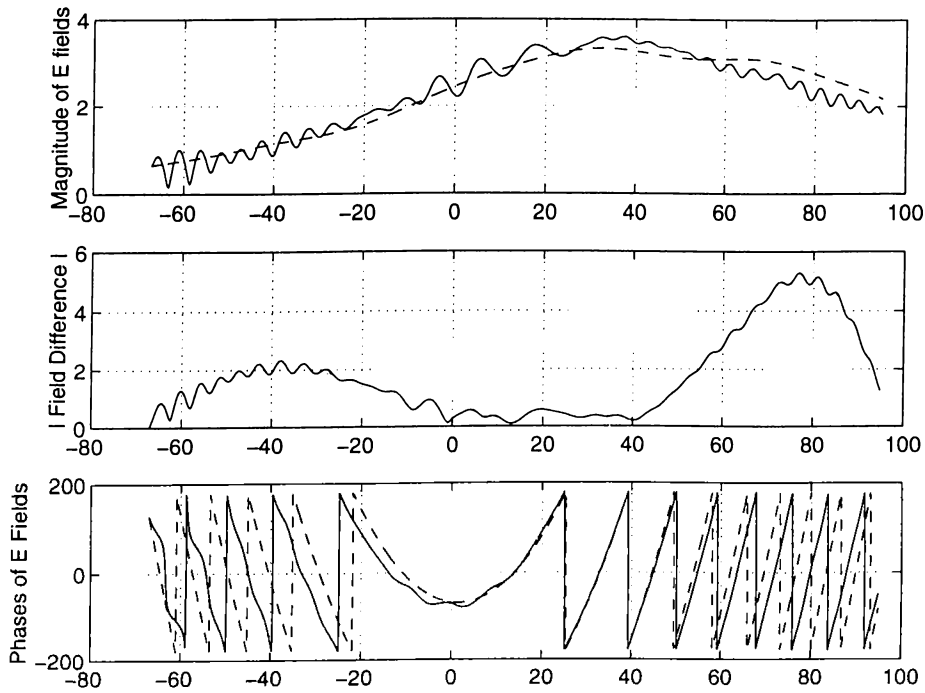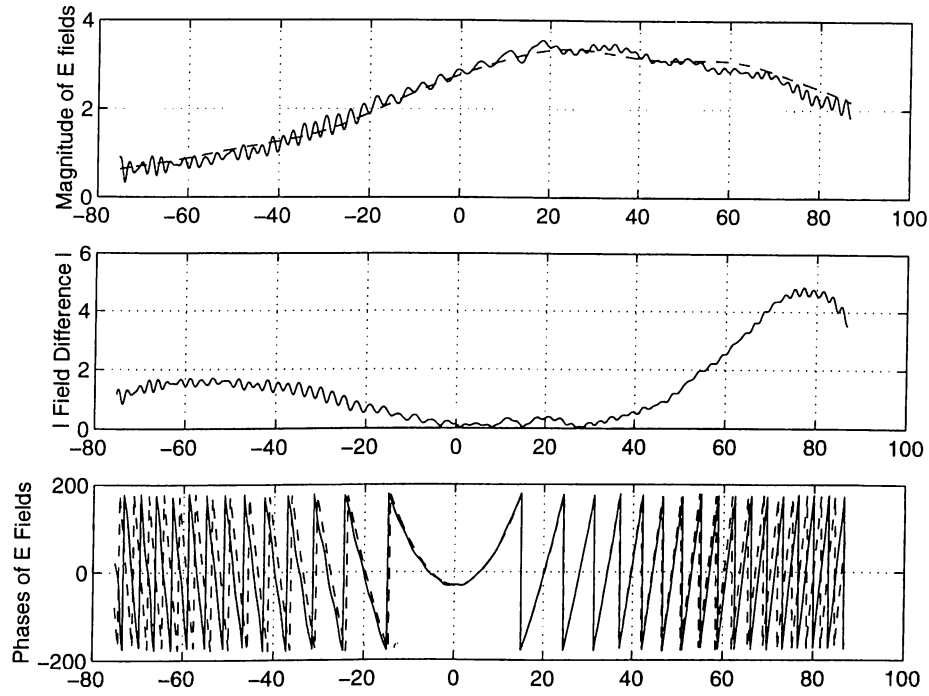


Figure 5.5: Far Fields of Radome (solid curve) and Slab (dashed curve) as functions of $\theta$ (E Polarization, Normal Incidence, $c = 10\lambda$, $\beta_{Radome} = \beta_{Slab} = 0°$, $\alpha = \theta - \beta_{Radome}$)
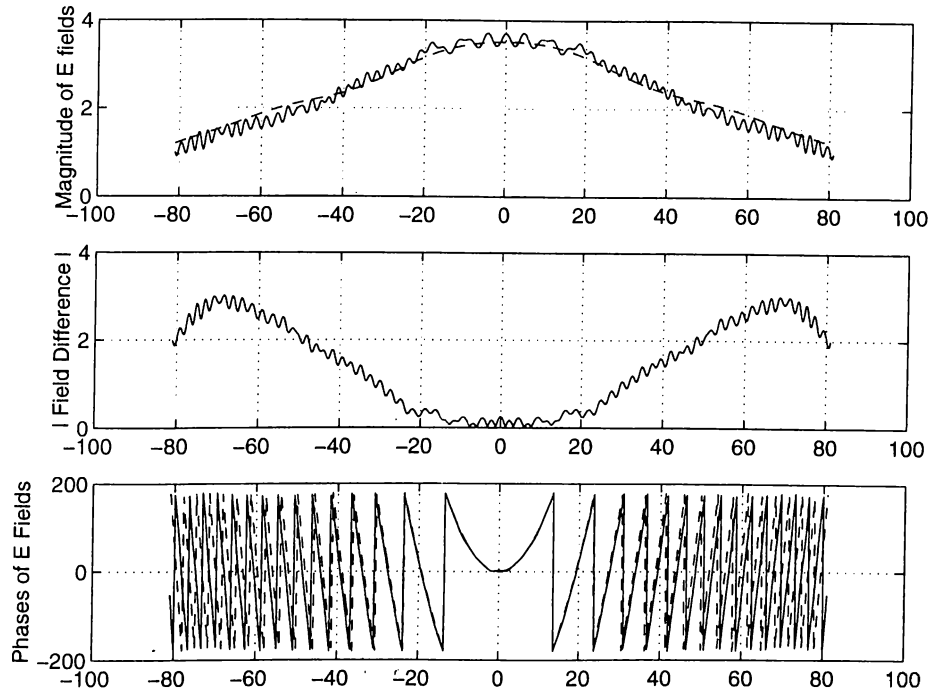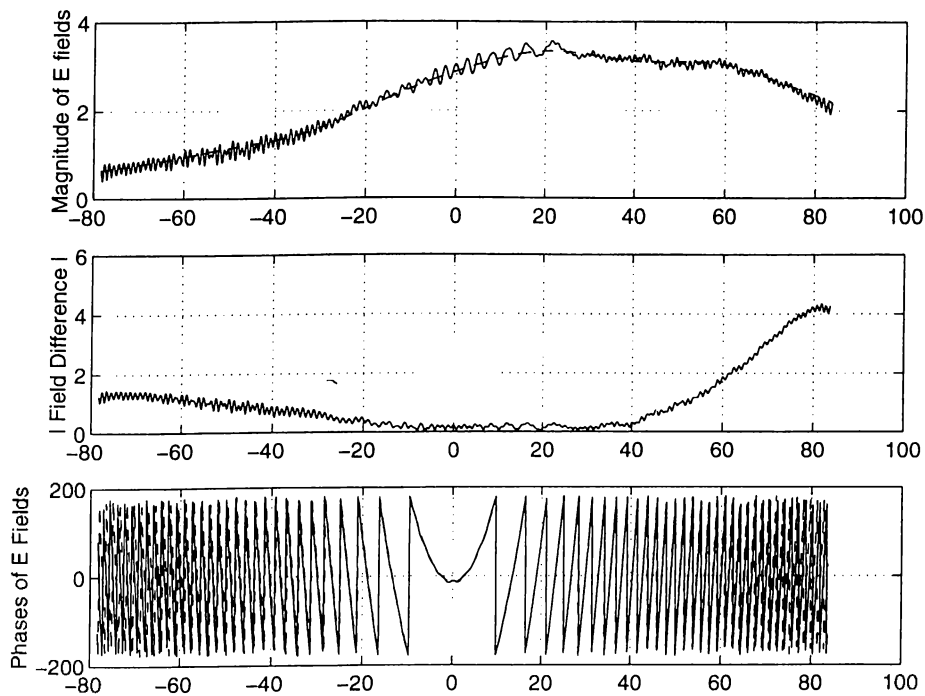
Figure 5.6: Far Fields of Radome (solid curve) and Slab (dashed curve) as functions of $\theta$ (E Polarization, Normal Incidence, $c = 20\lambda$, $\beta_{Radome} = \beta_{Slab} = 0^o$, $\alpha = \theta - \beta_{Radome}$)
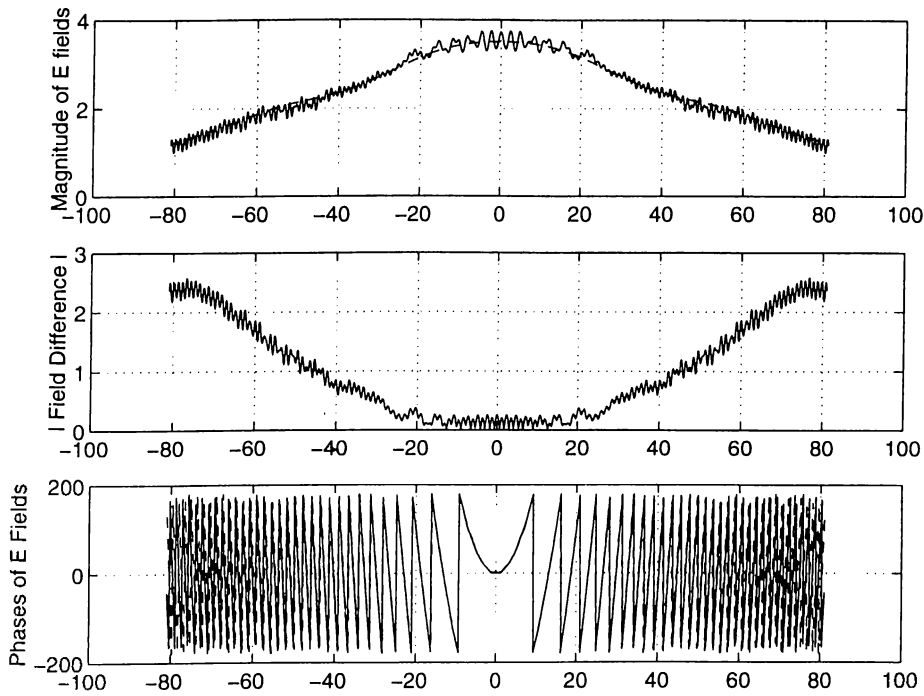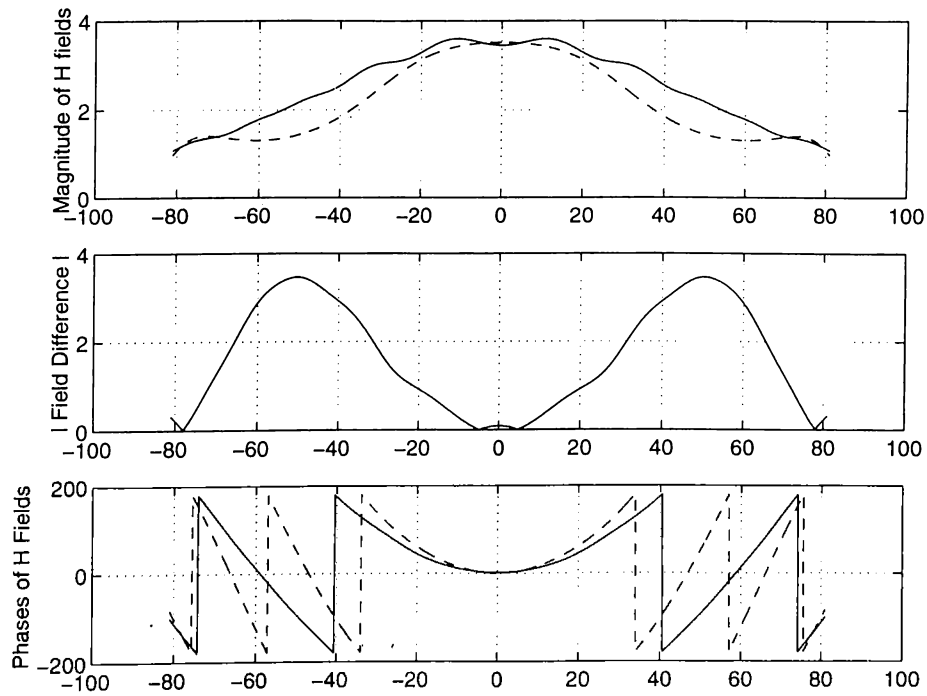


Figure 5.7: Far Fields of Radome (solid curve) and Slab (dashed curve) as functions of $\theta$ (E Polarization, Normal Incidence, $c = 40\lambda$, $\beta_{Radome} = \beta_{Slab} = 0^o$, $\alpha = \theta - \beta_{Radome}$)
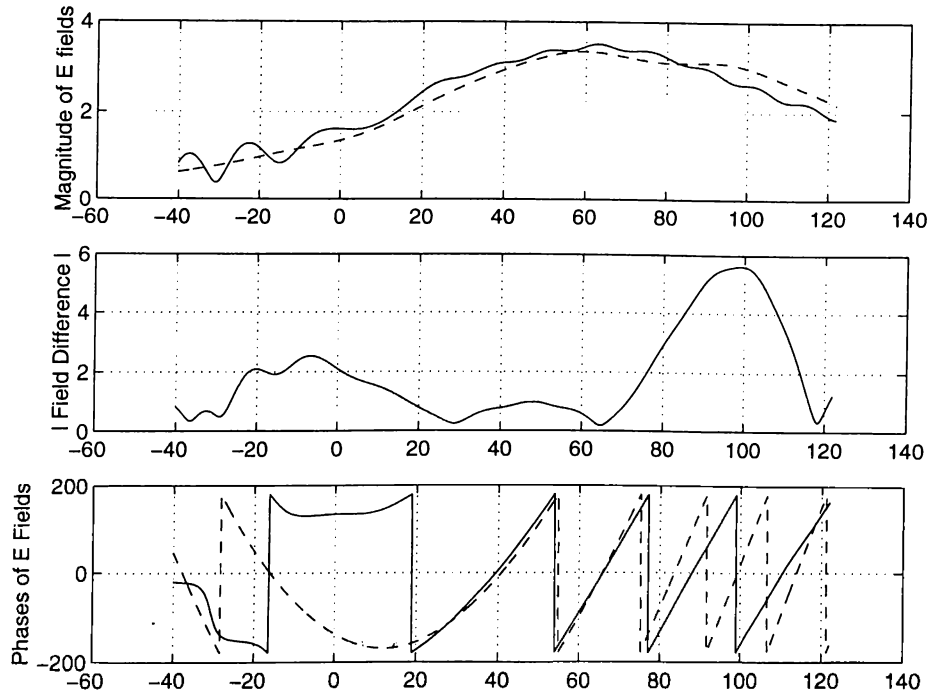
Figure 5.8: Far Fields of Radome (solid curve) and Slab (dashed curve) as functions of $\theta$ (E Polarization, Inclined Incidence, $c = 5\lambda$, $\beta_{Slab} = 30°$, $\alpha = \theta - \beta_{Radome}$)
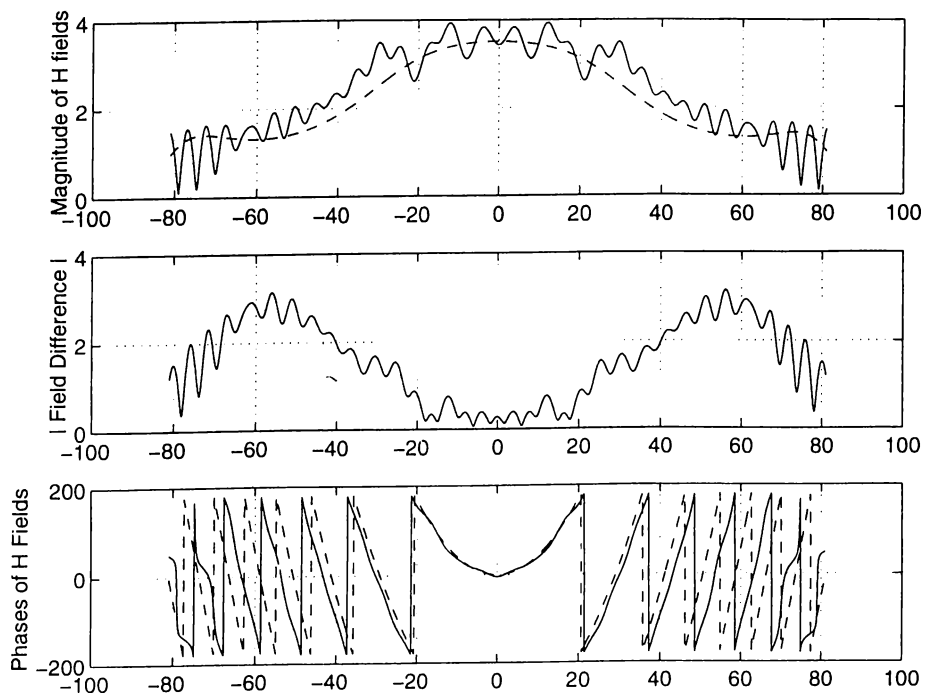


Figure 5.9: Far Fields of Radome (solid curve) and Slab (dashed curve) as functions of $\theta$ (E Polarization, Inclined Incidence, $c = 10\lambda$, $\beta_{Slab} = 30°$, $\alpha = \theta - \beta_{Radome}$)

Figure 5.10: Far Fields of Radome (solid curve) and Slab (dashed curve) as functions of $\theta$ (E Polarization, Inclined Incidence, $c = 20\lambda$, $\beta_{Slab} = 30^o$, $\alpha = \theta - \beta_{Radome}$)



Figure 5.11: Far Fields of Radome (solid curve) and Slab (dashed curve) as functions of $\theta$ (E Polarization, Inclined Incidence, $c = 40\lambda$, $\beta_{Slab} = 30^o$, $\alpha = \theta - \beta_{Radome}$)

Figure 5.12: Far Fields of Radome (solid curve) and Slab (dashed curve) as functions of $\theta$ (H Polarization, Normal Incidence, $c = 5\lambda$, $\beta_{Slab} = 0^o$, $\alpha = \theta - \beta_{Radome}$)



Figure 5.13: Far Fields of Radome (solid curve) and Slab (dashed curve) as functions of $\theta$ (H Polarization, Normal Incidence, $c = 10\lambda$, $\beta_{Slab} = 0^o$, $\alpha = \theta - \beta_{Radome}$)
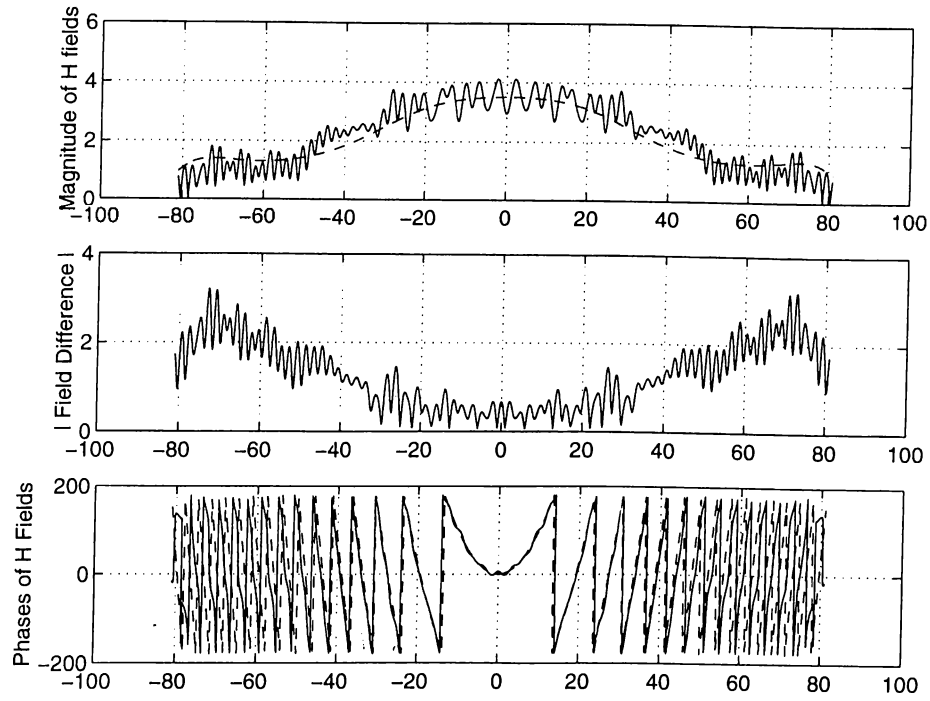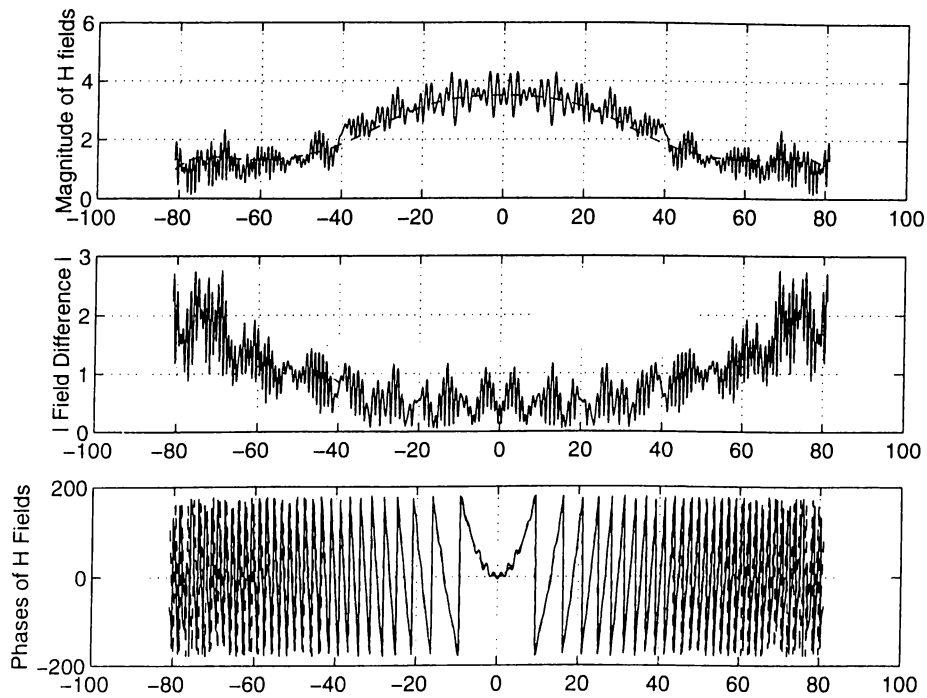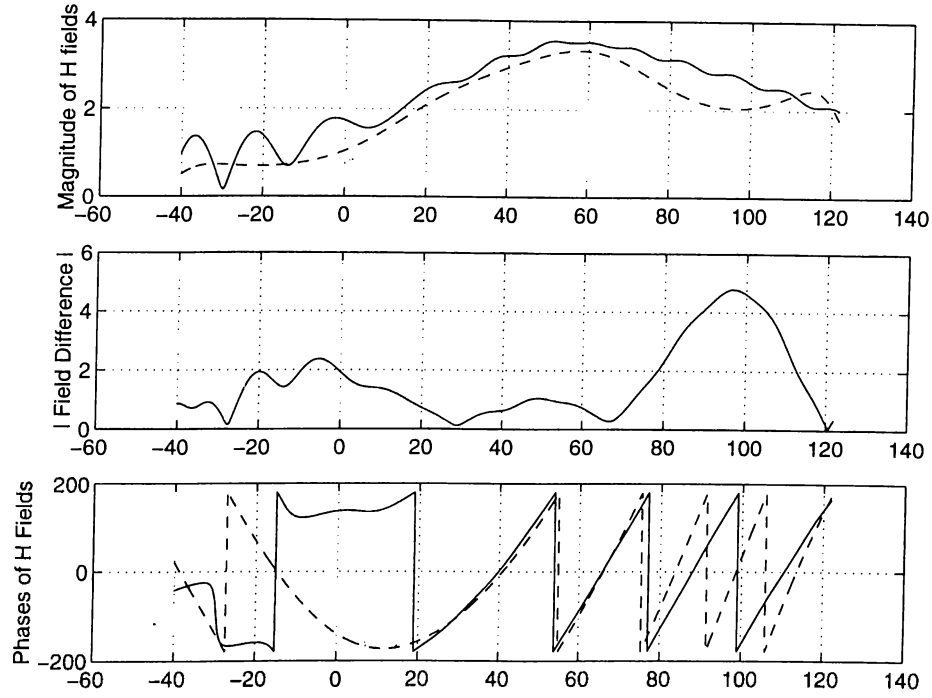
Figure 5.14: Far Fields of Radome (solid curve) and Slab (dashed curve) as functions of $\theta$ (H Polarization, Normal Incidence, $c = 20\lambda$, $\beta_{Slab} = 0°$, $\alpha = \theta - \beta_{Radome}$)



Figure 5.15: Far Fields of Radome (solid curve) and Slab (dashed curve) as functions of $\theta$ (H Polarization, Normal Incidence, $c = 40\lambda$, $\beta_{Slab} = 0°$, $\alpha = \theta - \beta_{Radome}$)
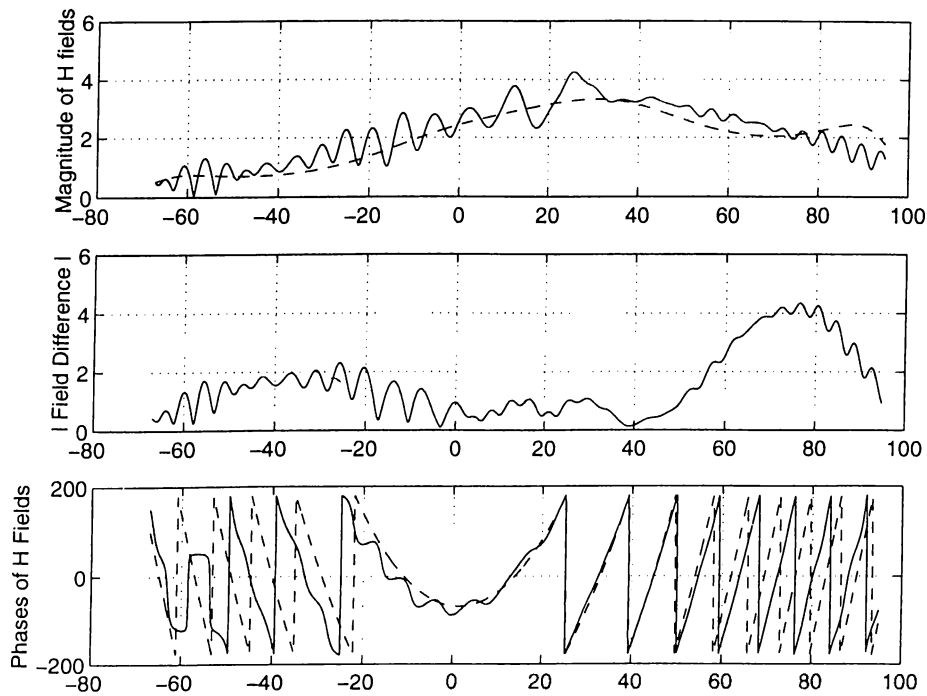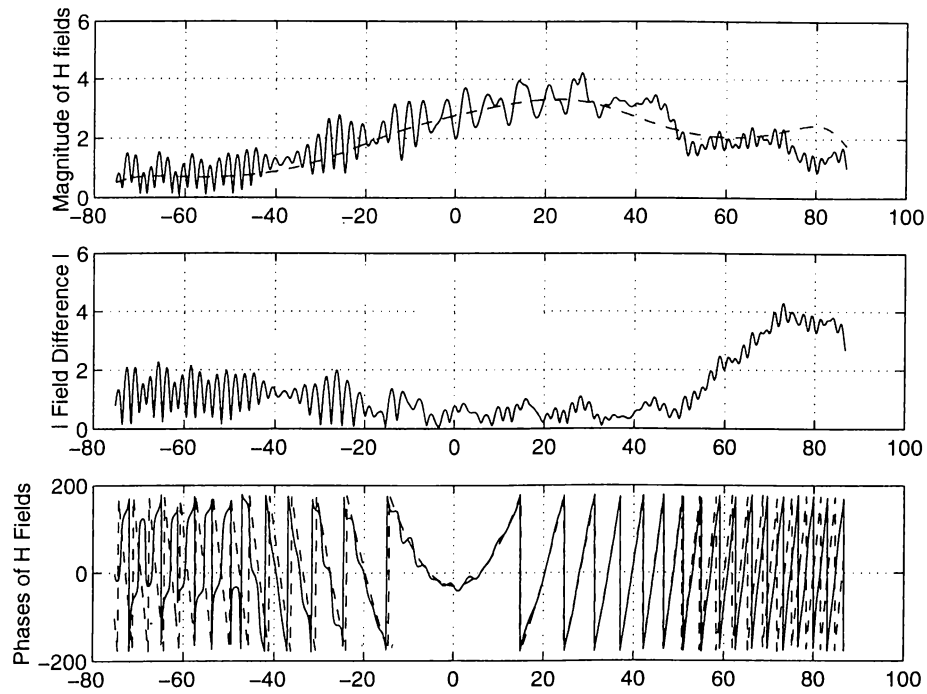
Figure 5.16: Far Fields of Radome (solid curve) and Slab (dashed curve) as functions of $\theta$ (H Polarization, Inclined Incidence, $c = 5\lambda$, $\beta_{Slab} = 30°$, $\alpha = \theta - \beta_{Radome}$)



Figure 5.17: Far Fields of Radome (solid curve) and Slab (dashed curve) as functions of $\theta$ (H Polarization, Inclined Incidence, $c = 10\lambda$, $\beta_{Slab} = 30°$, $\alpha = \theta - \beta_{Radome}$)
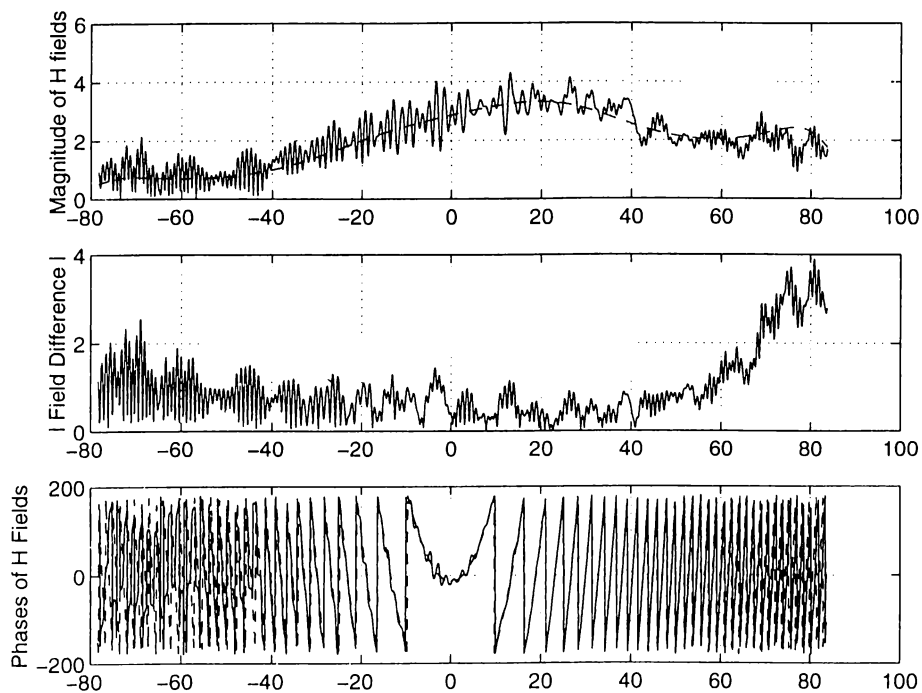
Figure 5.18: Far Fields of Radome (solid curve) and Slab (dashed curve) as functions of $\theta$ (H Polarization, Inclined Incidence, $c = 20\lambda$, $\beta_{Slab} = 30°$, $\alpha = \theta - \beta_{Radome}$)



Figure 5.19: Far Fields of Radome (solid curve) and Slab (dashed curve) as functions of $\theta$ (H Polarization, Inclined Incidence, $c = 10\lambda$, $\beta_{Slab} = 30°$, $\alpha = \theta - \beta_{Radome}$)
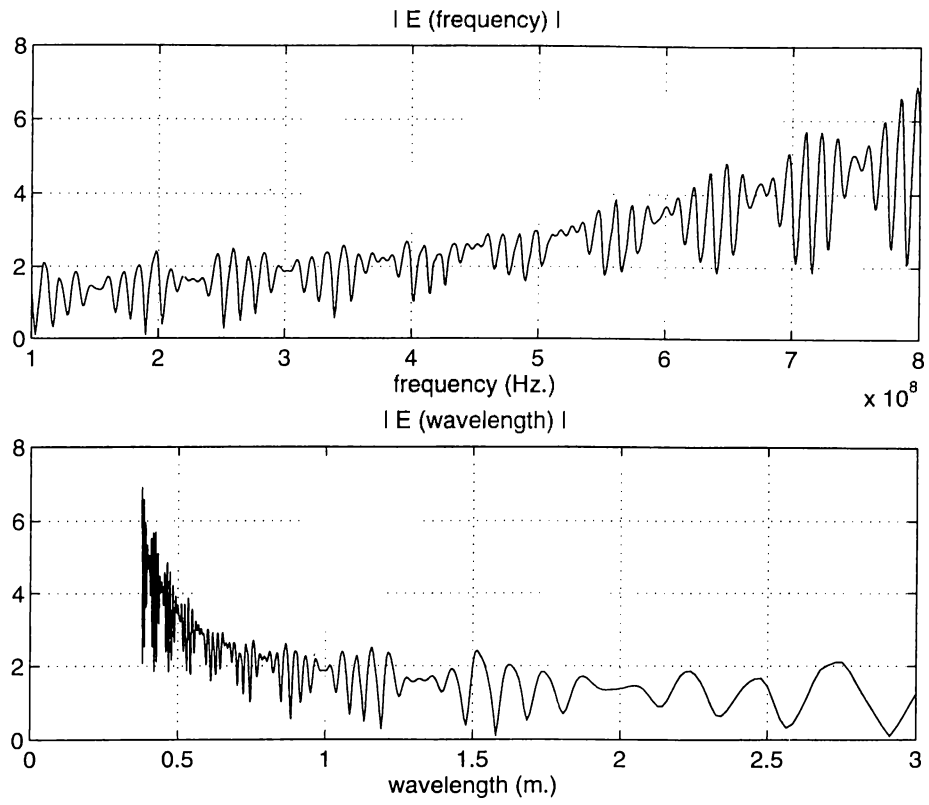
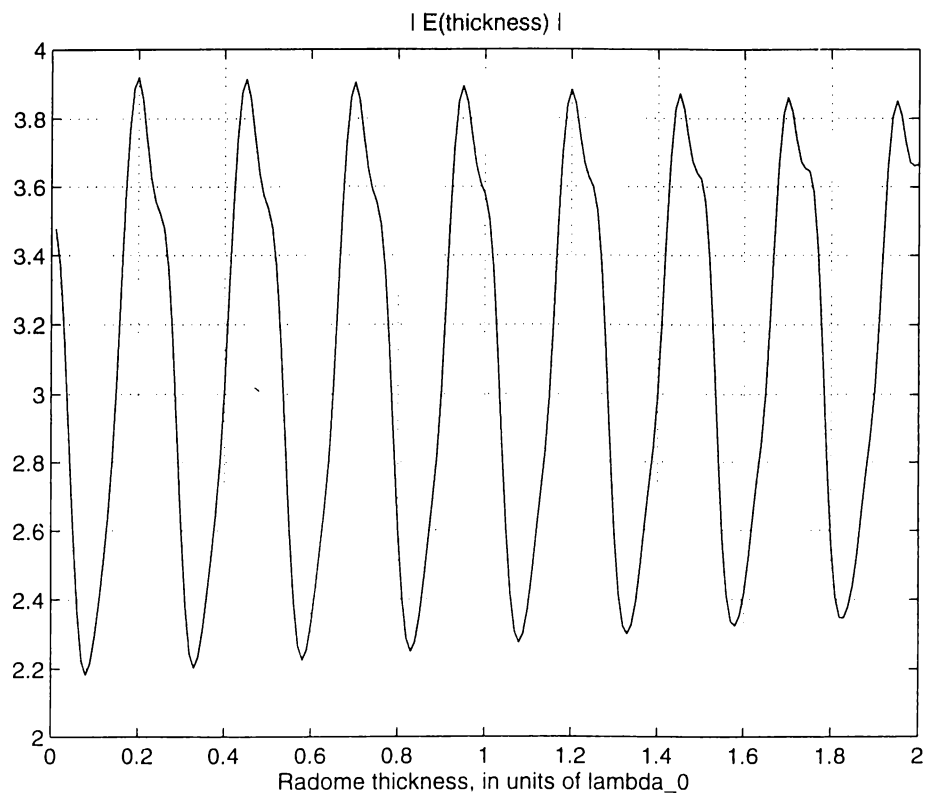Figure 5.20: Far field as a function of frequency and wavelength



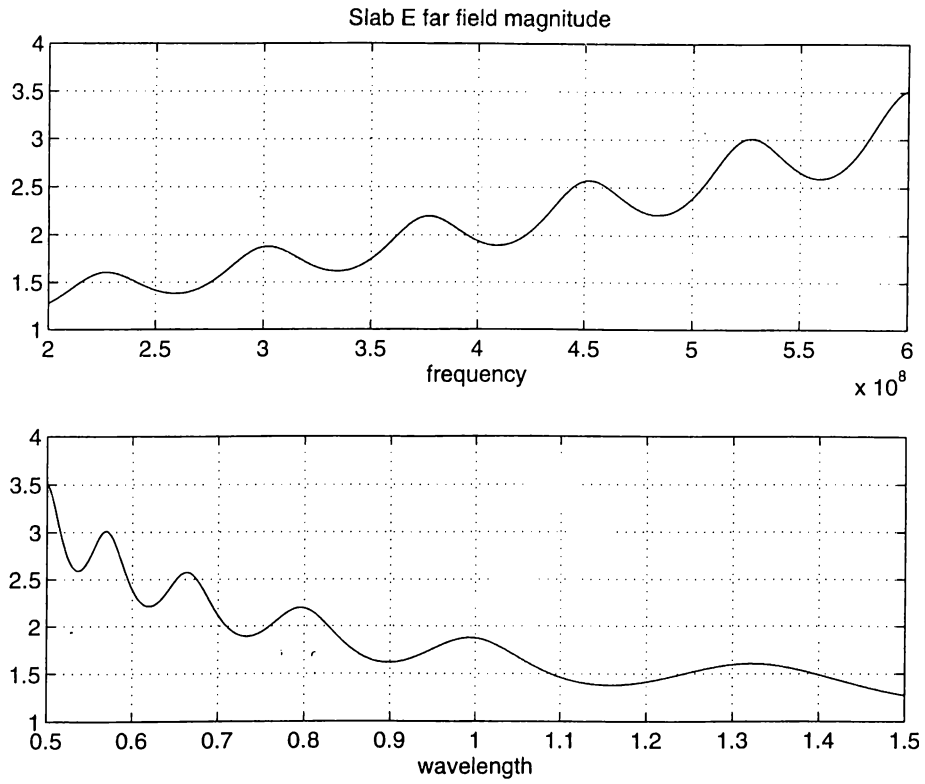Figure 5.21: Far field as a function of the radome thickness

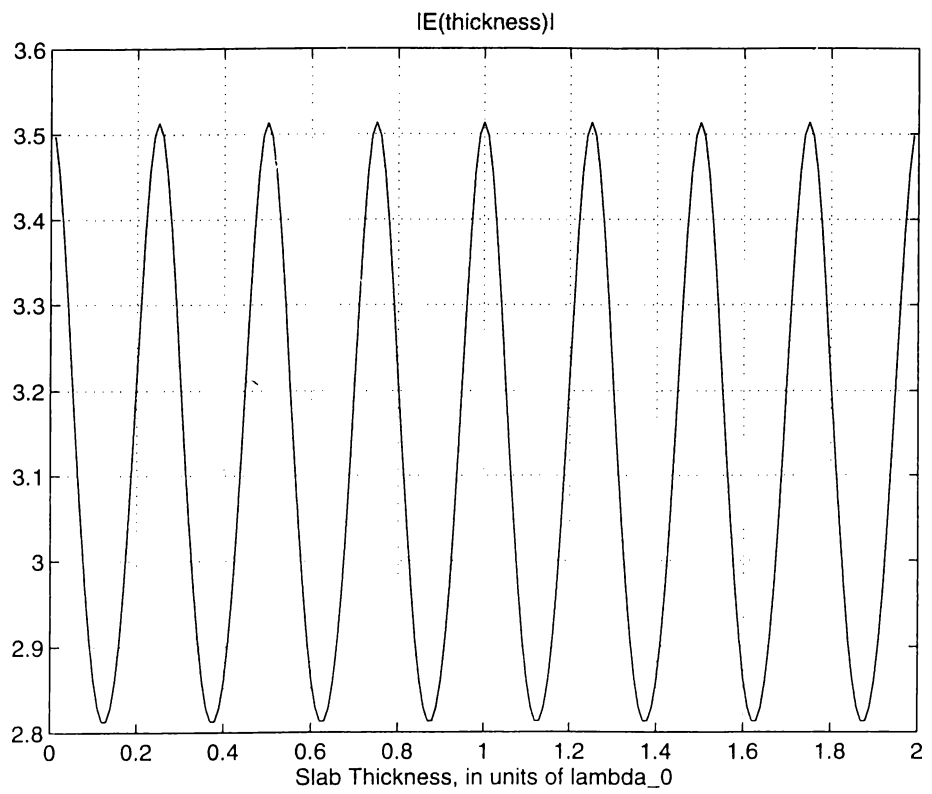Figure 5.22: Far field as a function of frequency and wavelength



Figure 5.23: Far field as a function of the slab thickness

# REFERENCES

[1] Jeng-Hwa Chang and Kuan-Kin Chan "Analysis of a Two-Dimensional Radome of Arbitrary Curved Surface," *IEEE Trans. AP.*, vol. 38, pp. 1565-1568, Oct. 1990.

[2] Pinchas D. Einziger and Leopold B. Felsen "Rigorous Asymptotic Analysis of Transmission Through a Curved Dielectric Slab," *IEEE Trans. AP.*, vol. 31, pp. 863-870, Nov. 1983.

[3] X. J. Gao and Leopold B. Felsen "Complex Ray Analysis of Beam Transmission Through Two-Dimensional Radomes," *IEEE Trans. AP.*, vol. 33, pp. 963-975, Sept. 1985.

[4] John J. Maciel and Leopold B. Felsen "Gaussian Beam Analysis of Propagation from an Extended Plane Aperture Distribution Through Dielectric Layers, Part I - Plane Layer, Part II - Circular Cylindrical Layer," *IEEE Trans. AP.*, vol. 38, pp. 1607-1624, Oct. 1990.

[5] Leopold B. Felsen, N. Subramaniam and K. Arichandran "Equivalence Relation Between Partial Angular Harmonic and Ray-Type Green's Functions for a Cylindrical Dielectric Layer," *IEEE Trans. AP.*, vol. 38, pp. 1273-1279, Aug. 1990.

[6] J. W. Ra, H. L. Bertoni and Leopold B. Felsen "Reflection and Transmission of Beams at a Dielectric Interface," *SIAM J. Appl. Math.*, vol. 24, No.3 pp. 396-413, May. 1973.

[7] Leopold B. Felsen "Complex-Source-Point Solutions of the Field Equations and their Relation to the Propagation and Scattering of Gaussian Beams," pp. 39-56.

[8] Cornelis F. Du Toit "The Numerical Computation of Bessel Functions of the First and Second Kind for Integer Orders and Complex Arguments," *IEEE Trans. AP.*, vol. 38, pp. 1341-1349, Sep. 1990.

[9] Milton Abramowitz and Irene A. Stegun "Handbook of mathematical functions, with formulas, graphs, and mathematical tables," *New York, Dover Publications, 1972*

[10] Cornelis F. Du Toit "Evaluation of Some Algoritms and Programs for the Computation of Integer-Order Bessel Functions of the First and Second Kind with Complex Arguments," *IEEE AP Magazine*, vol. 35, pp. 19-25, June 1993.

[11] Weng Cho Chew "Waves and Fields in Inhomogeneous Media," *IEEE Press, 1995.*

[12] Jin Au Kong "Electromagnetic Wave Theory," *A Wiley-Interscience Publication*

[13] F. B. Hildebrand "Introduction to Numerical Analysis," *Dover Publications, 1974.*

[14] Shepley L. Ross "Differential Equations," Wiley, 3rd Edition.